

1 FORESAIL-1 cubesat mission to measure radiation belt 2 losses and demonstrate de-orbiting

3 M. Palmroth^{1,2}, J. Praks³, R. Vainio⁴, P. Janhunen², E. K. J. Kilpua¹, N. Yu.
4 Ganushkina^{2,5}, A. Afanasiev⁴, M. Ala-Lahti¹, A. Alho³, T. Asikainen⁶,
5 E. Asvestari¹, M. Battarbee¹, A. Binios³, A. Bosser³, T. Brito¹, J. Envall²,
6 U. Ganse¹, H. George¹, J. Gieseler⁴, S. Good¹, M. Grandin¹, S. Haslam²,
7 H.-P. Hedman⁷, H. Hietala⁴, N. Jovanovic³, S. Kakakhel⁷, M. Kalliokoski¹,
8 V. V. Kettunen³, T. Koskela^{1,4}, E. Lumme¹, M. Meskanen², D. Morosan¹,
9 M. Rizwan Mughal³, P. Niemelä³, S. Nyman³, P. Oleynik⁴, A. Osmane¹,
10 E. Palmerio¹, Y. Pfau-Kempf¹, J. Peltonen⁴, J. Plosila⁷, J. Polkko²,
11 S. Poluianov^{6,8}, J. Pomoell¹, D. Price¹, A. Punkkinen⁴, R. Punkkinen⁷,
12 B. Riwanto³, L. Salomaa⁷, A. Slavinskis^{3,9}, T. Sääntti⁷, J. Tammi⁷,
13 H. Tenhunen⁷, P. Toivanen², J. Tuominen⁷, L. Turc¹, E. Valtonen⁴,
14 P. Virtanen⁴, T. Westerlund⁷

15 ¹University of Helsinki, Department of Physics, Helsinki, Finland

16 ²Finnish Meteorological Institute, Space and Earth Observation Centre, Helsinki, Finland

17 ³Aalto University, School of Electrical Engineering, Espoo, Finland

18 ⁴University of Turku, Department of Physics and Astronomy, Turku, Finland

19 ⁵University of Michigan, Department of Climate and Space Sciences and Engineering, Ann Arbor, USA

20 ⁶University of Oulu, Space Climate Research Unit, Oulu, Finland

21 ⁷University of Turku, Department of Future Technologies, Turku, Finland

22 ⁸University of Oulu, Sodankylä Geophysical Observatory (Oulu Unit), Oulu, Finland

23 ⁹University of Tartu, Tartu Observatory, Tõravere, Estonia

24 Key Points:

- 25 • FORESAIL-1 mission measures energetic electron precipitation and solar energetic
26 neutral atom flux
- 27 • We will demonstrate a cost-efficient de-orbiting and orbit manoeuvring technol-
28 ogy without propellants
- 29 • The goal of the mission is to contribute significantly to the sustainable utilisation
30 of space

This is the author manuscript accepted for publication and has undergone full peer review but has not been through the copyediting, typesetting, pagination and proofreading process, which may lead to differences between this version and the [Version of Record](#). Please cite this article as doi: [10.1029/2018JA026354](https://doi.org/10.1029/2018JA026354)

Corresponding author: Minna Palmroth, minna.palmroth@helsinki.fi

Abstract

Today, the near-Earth space is facing a paradigm change as the number of new spacecraft is literally sky-rocketing. Increasing numbers of small satellites threaten the sustainable use of space, as without removal, space debris will eventually make certain critical orbits unusable. A central factor affecting small spacecraft health and leading to debris is the radiation environment, which is unpredictable due to an incomplete understanding of the near-Earth radiation environment itself and its variability driven by the solar wind and outer magnetosphere. This paper presents the FORESAIL-1 nanosatellite mission, having two scientific and one technological objectives. The first scientific objective is to measure the energy and flux of energetic particle loss to the atmosphere with a representative energy and pitch angle resolution over a wide range of magnetic local times. To pave the way to novel model - *in situ* data comparisons, we also show preliminary results on precipitating electron fluxes obtained with the new global hybrid-Vlasov simulation Vlasiator. The second scientific objective of the FORESAIL-1 mission is to measure energetic neutral atoms (ENAs) of solar origin. The solar ENA flux has the potential to contribute importantly to the knowledge of solar eruption energy budget estimations. The technological objective is to demonstrate a satellite de-orbiting technology, and for the first time, make an orbit manoeuvre with a propellantless nanosatellite. FORESAIL-1 will demonstrate the potential for nanosatellites to make important scientific contributions as well as promote the sustainable utilisation of space by using a cost-efficient de-orbiting technology.

1 Introduction

Unprecedented numbers of new spacecraft are now being launched into Earth orbit to satisfy the growing demand from the scientific, commercial, and military sectors. Most of these new spacecraft need to survive in the radiation belts (RBs; van Allen & Frank, 1959), which are regions of trapped energetic charged particles. The RBs are critical in terms of space weather, as the radiation ages the spacecraft and deteriorates hardware. All new satellites contribute to the already existing large number of orbital debris, if they are not actively removed at the end of the mission. This section introduces the state of the art in the three scientific and technological objectives of the FORESAIL-1 mission: measurements of energetic particle precipitation and solar energetic neutral atoms (ENAs), and de-orbiting technologies.

1.1 State of the Art: Electron precipitation observations

The RBs are produced by a complex balance of particle source and loss processes that vary both temporally and spatially (e.g., Tverskoy, 1969; Walt, 1996; Chen et al., 2007; Shprits et al., 2008; Thorne, 2010). Significant variations in electron fluxes occur over various time scales as a function of both energy and distance, driven by solar-magnetospheric interactions and internal magnetospheric processes (e.g., Li et al., 1997; Elkington et al., 2003; Reeves et al., 2003; Shprits et al., 2006; Baker & Kanekal, 2008). Effective losses from the outer radiation belts consist of 1) loss through the outer edge of the magnetosphere (magnetopause shadowing (e.g., West et al., 1972; Ukhorskiy et al., 2006; Saito et al., 2010; Matsumura et al., 2011; Turner et al., 2014)), 2) radial outward displacement of the electrons due to waves (Mann et al., 2016), and weakening of the Earth's magnetic field (the D_{st} effect (McIlwain (1966); Kim & Chan (1997); Millan & Thorne (2007))), and 3) wave-particle interactions resulting in scattering of particles into the loss cone (Kennel & Petschek, 1966; Thorne & Kennel, 1971; Thorne, 1974). There are no comprehensive estimates about which of these processes is most important during different conditions, while it is clear that particle losses play a central part in regulating the RBs.

80 The wave-particle interactions leading to losses from the RBs vary on time scales
81 ranging from 100 milliseconds to several minutes (Millan & Thorne, 2007). Balloon ex-
82 periments have historically been the earliest method to determine this loss category by
83 measuring the X-rays from bremsstrahlung radiation induced by the interaction of pre-
84 cipitating particles with the neutrals in the upper atmosphere (Barcus et al., 1973; Pytte
85 et al., 1976). Latest such observations are provided by the BARREL mission (Millan &
86 the BARREL Team, 2011; Woodger et al., 2015). All balloon missions are constrained
87 to balloon-reachable altitudes and thus only allow indirect observation of the precipitat-
88 ing particles.

89 Energetic particle precipitation has also been observed from the ground, as precip-
90 itating electrons with energies over several tens of keV cause enhanced ionisation in the
91 ionospheric D-region at an altitude of about 90 km. Relative ionospheric opacity meters
92 (riometers) (Hargreaves, 1969) are ground-based passive radars measuring the so-called
93 cosmic noise absorption (Shain, 1951), which corresponds to absorbed radio wave power
94 in the ionosphere resulting from enhanced D-region electron density. Recently, interfer-
95 ometric riometry has been developed to produce all-sky maps (e.g. McKay-Bukowski et
96 al., 2015). Ground-based observations of energetic electron precipitation can also be achieved
97 using incoherent scatter radars, which can accurately measure D-region electron density
98 down to about 70 km altitude (e.g. Miyoshi et al., 2015). However, the intrinsically in-
99 direct ground-based observations do not allow inferring precipitating particle fluxes and
100 energies, even using newly developed approaches such as spectral riometry (Kero et al.,
101 2014). Hence having direct measurements of precipitating fluxes from space-borne in-
102 struments is critical for radiation belt loss studies.

103 One of the first satellite missions to study energetic electron precipitation was the
104 Solar, Anomalous, and Magnetospheric Particle Explorer (SAMPEX, 1992 - 2012) used
105 in a number of studies (Li et al., 2001; Tu et al., 2010; Nakamura et al., 2000). DEME-
106 TER microsatellite observed electron fluxes at energies between 70 keV and 2.5 MeV with
107 high energy resolution (256 channels) on a 700 km orbit (Sauvaud et al., 2006). These
108 observations have been used to infer energetic electron precipitation (Graf et al., 2009),
109 although DEMETER viewed primarily trapped particles. The main data set of direct
110 measurements of precipitating energetic particles comes from the Medium Energy Pro-
111 ton and Electron Detector (MEPED) onboard NOAA/POES satellites (D. S. Evans &
112 Greer, 2000). MEPED consists of two telescopes, the 0° telescope designed to measure
113 precipitating particle fluxes and the 90° telescope for trapped particle fluxes, measur-
114 ing electrons in three energy channels (>30 keV, >100 keV, and >300 keV) and protons
115 in five energy channels (>30 keV, >80 keV, >250 keV, >800 keV, and >2.5 MeV). How-
116 ever, the NOAA/POES particle data suffer from two issues. First, the 0° telescope only
117 partially views the bounce loss cone and does not offer any angular resolution inside its
118 viewcone leading to poor pitch angle resolution. This leads to an underestimation of the
119 precipitating fluxes (Rodger et al., 2013). Second, the electron channels are affected by
120 proton contamination; partly corrected by a new data set by Asikainen & Mursula (2013).

121 Particle precipitation is a key element in magnetosphere–ionosphere–thermosphere
122 coupling, and therefore a crucial objective for research in numerical models, especially
123 as there is an increasing demand for space weather forecasting capabilities. The first at-
124 tempts to model precipitating particle fluxes relied on statistical patterns inferred from
125 satellite observations. McDiarmid et al. (1975) produced a model for precipitating elec-
126 tron flux within 0.15–200 keV as a function of magnetic local time (MLT) and invari-
127 ant latitude based on about 1100 passes of the ISIS 2 spacecraft. Using data measured
128 by the Low Energy Electron experiment onboard the Atmosphere Explorer C and D satel-
129 lites, Spiro et al. (1982) parametrised precipitating electron energy flux and average en-
130 ergy as a function of MLT, geomagnetic latitude, and geomagnetic activity measured by
131 the Kp and AE indices. One of the reference models for auroral-energy electron precip-
132 itation is the Hardy et al. (1985) model, empirically derived by compiling several years

of observations from the Defense Meteorological Satellite Program and Satellite (DMSP) Test Program spacecraft. The Hardy model is parametrised by the Kp index, and it is still used to provide precipitation input in the 50 eV–20 keV energy range to state-of-the-art ionospheric models (e.g., Marchaudon & Blelly, 2015). At higher energies (30 keV–1 MeV), the recent van de Kamp et al. (2016) model provides energy-flux spectra of precipitating electrons as a function of L parameter and geomagnetic activity rendered with the Ap index. This empirical model was obtained from a statistical analysis of 11 years of NOAA/POES energetic electron precipitation observations and is averaged across all MLTs in its present version.

Modelling particle precipitation using first-principle models is not easy, given that many processes operating at spatial and temporal scales spanning many orders of magnitude are at play in the inner magnetosphere (energisation, and loss-cone scattering processes, among others). The emergence of global kinetic magnetospheric codes may enable addressing this issue in the near future. Recently, a preliminary run was performed using the Vlasiator code (von Althaus et al., 2014; Palmroth et al., 2018), in which electrons were added as a modelled species during a substorm-time, polar-plane global magnetospheric run throughout the magnetospheric simulation box. Figure 1 shows an example of these preliminary results of 0.1 – 60 keV electron precipitation estimation obtained from the analysis of the nightside velocity distribution functions of electrons at a single time step of this simulation. The top panel shows the differential number flux of precipitating electrons as a function of L shell (blue shading), as well as the mean precipitating energy (black line) in the same units as typical spacecraft data. The bottom panel shows the integral energy flux as a function of L . The integral energy flux was obtained by multiplying the differential number flux by the corresponding energies, and integrating across energies. The mean precipitating energy was calculated by dividing the integral energy flux by the total number flux (i.e., the differential number flux integrated across energies). The Hardy et al. (1985) model predicts a maximum integral energy flux of the order of $108 - 109 \text{ keV cm}^{-2} \text{ s}^{-1} \text{ sr}^{-1}$ in the midnight sector, reached at geomagnetic latitudes comprised between 62° and 69° (translating into L values between 4.5 and 7.8), depending on geomagnetic activity given by the Kp index. The preliminary results from Vlasiator in Fig. 1 are therefore in reasonable agreement with those values.

With the expanding human activity in space, it is increasingly important to measure precipitating particle fluxes *in situ* and predict the precipitation by modelling, in order to understand the Earth’s radiation environment. While previous satellite missions have provided a plethora of observations of the physical processes within the precipitation environment, none of the missions were designed specifically with a clear focus on precipitation. A number of new cubesat missions recently launched or being built focus on precipitation. These include, for example, the CSSWE mission (Kohnert et al., 2011), the ELFEN mission (Shprits et al., 2018), the Firebird mission Crew et al. (2016), and the AMICal Sat mission (Barthelemy et al., 2018). FORESAIL-1 will be a complementary mission, improving the spatial and temporal resolution of precipitation that may be offered by these missions together.

1.2 State of the Art: Solar energetic neutral atom observations

The energy budgets of the solar corona and solar eruptions are major unsolved questions in solar physics. Coronal heating leads to an abundance of suprathermal particles in the corona. Suprathermal ions are important for estimating the energy budget of an eruption (e.g., Emslie et al., 2004), however, they do not produce measurable amounts of electromagnetic radiation, and thus their abundance is difficult to measure. Direct *in situ* measurements of suprathermal ions will be provided by the recently launched NASA Parker Solar Probe mission, but only within the outermost reaches of the solar corona. During solar eruptions these suprathermal ions can be driven to participate in charge exchange processes with neutral atoms, resulting in the formation of solar energetic neu-

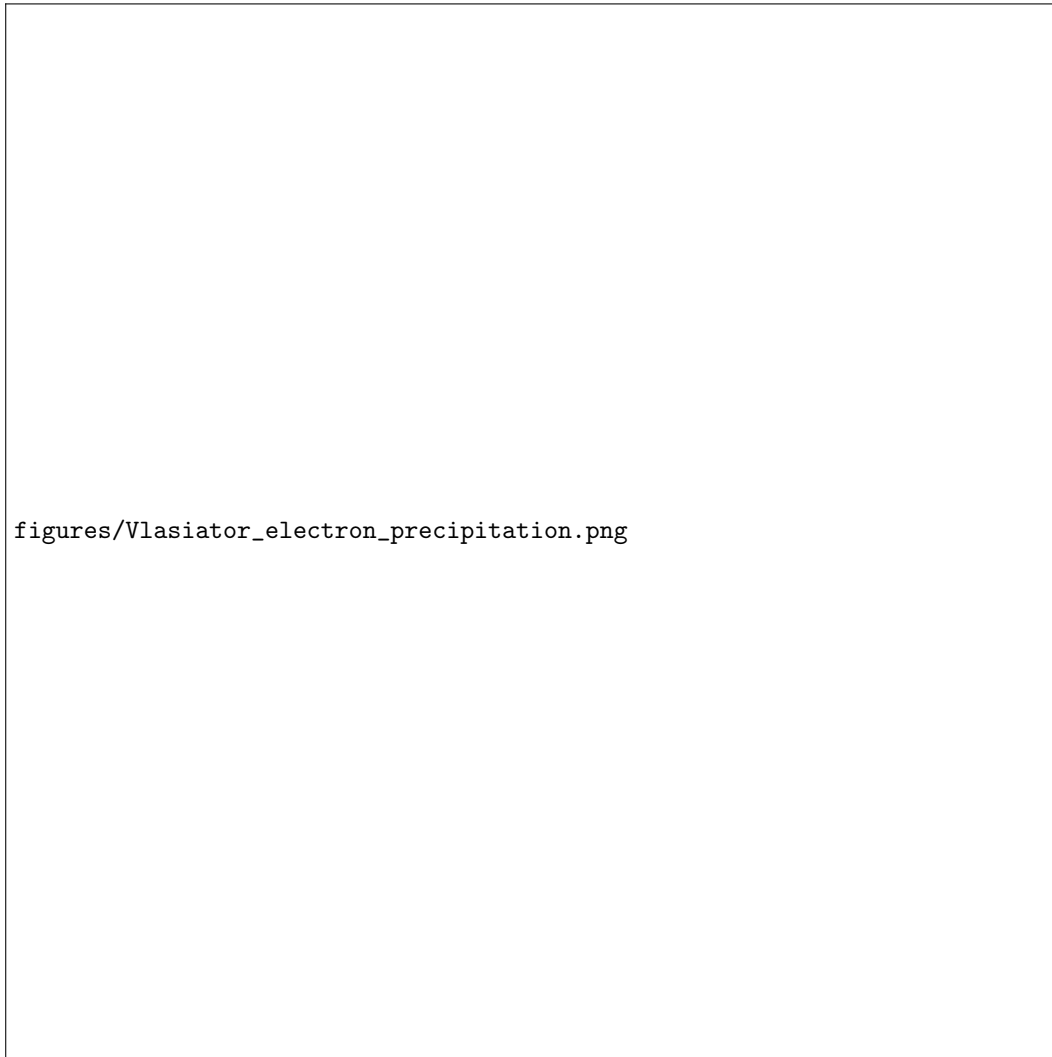


Figure 1. Preliminary results of Vlasiator modelling of electron precipitation. (top) Differential flux of precipitating electrons as a function of L shell, in the same units as usually measured by telescopes onboard spacecraft. The black line indicates the mean precipitating energy. (bottom) Total precipitating energy flux as a function of L shell.

185 tral atoms (ENAs). So far, ENAs have been measured only during one single event (Mewaldt
186 et al., 2009) with the IMPACT/LET instrument onboard the twin the Solar TERrestrial
187 RELations Observatory (STEREO) spacecraft close to the beginning of the mission. Even
188 these results may be questionable, as they have been disputed by Simnett (2011), who
189 suggested the ENA observations could be explained by an earlier precursor event, de-
190 tected as an electron burst.

191 **1.3 State of the Art: Space debris removal technologies**

192 The number of spacecraft in low-Earth orbit (LEO) is rapidly increasing, as tech-
193 nological and regulatory changes of launchers have allowed smaller satellites. These so-
194 called nanosatellites typically do not have propulsion systems requiring bulky or volatile
195 propellants for orbit control or de-orbiting, making them a significant source of future
196 orbital debris. Furthermore, if they cannot handle high-radiation environments, these
197 nanosatellites will fail early, thus on one hand contributing to existing debris and on the
198 other hand defeating potential plans for active deorbiting at the end of mission. The sus-
199 tainable use of the near-Earth space has become of great interest (e.g., Bastida Virgili
200 et al., 2016). To avoid low-Earth orbits becoming unusable in the future, also nanosatel-
201 lites should be removed at end-of-life, otherwise the amount of space debris will increase
202 exponentially due to collisions with bigger objects (Kessler & Cour-Palais, n.d.; Klinkrad,
203 1993; Bradley & Wein, 2009; Bonnal et al., 2013), creating a potential danger to all later
204 space missions. International standards have been developed to impose requirements on
205 space missions to mitigate space debris production (e.g., European Space Agency, 2014;
206 for Standardization, 2011). Thus, it is crucial to develop robust instruments for both con-
207 trolling the small satellite orbits as well as for removing them from orbit after the end
208 of the mission.

209 Apart from technological solutions for reduction of space debris that are inherent
210 to the satellite design, efforts for third-party orbit removal techniques are ongoing. Ap-
211 proaches include spacecraft that perform automatic rendez-vous, attachment and joint
212 de-orbiting of larger space debris items. Using high-powered lasers (either ground- or satellite-
213 based) to exert radiation pressure, or directly ablate the surface material of space de-
214 bris (a so-called "Laser Broom") has been a research project in both civilian (Bekey, 1997;
215 Phipps et al., 2012) and military (Campbell, 2000) projects. Compact propulsion meth-
216 ods possibly allowing de-orbiting of nanosatellites include miniaturised pulsed plasma
217 and Hall-effect thrusters, which have reached commercial technological readiness, but
218 still require propellants and a sizeable energy budget (Tummala & Dutta, 2017). Pho-
219 tonic solar sails have been investigated for propellantless propulsion and used success-
220 fully for interplanetary missions (Tsuda et al., 2013), as well as multiple nanosatellite
221 missions (Lappas et al., 2011) with mixed success. Meanwhile, electric sails, in which elec-
222 trically charged structures interact with the ion environment, have been proposed (Jan-
223 hunen, 2004), and suitable packages have been implemented for nanosatellites, but suc-
224 cessful experimental verification is still outstanding.

225 **2 Science goals**

226 **2.1 Mission statement**

227 FORESAIL-1 is the first nanosatellite mission designed to measure the energy-dependent
228 pitch angle spectra of the precipitating radiation belt particles, and solar ENA flux. Fur-
229 ther, FORESAIL-1 will demonstrate the effectiveness of the plasma brake as a means
230 of manipulating the spacecraft orbit in operation and lowering the spacecraft altitude
231 to speed up de-orbiting at the end of the mission, thus addressing the sustainability of
232 LEO space operations.

2.2 Science objectives

The FORESAIL-1 mission answers the following science questions: What are the pitch-angle and energy signatures of precipitation events as a function of MLT? How is the precipitation pitch-angle and energy distribution dependent on geomagnetic activity and driving from the solar wind? Thus, the FORESAIL-1 mission aims to perform precise directional measurements of electron and proton precipitation, as well as the energy spectrum and particle fluxes over a wide energy range (tens of keV to approximately one MeV). The spacecraft orbit shall drift in magnetic local time to allow determining precipitation as a function of MLT. The time resolution needs to be good enough to describe the lower bound on precipitation budget due to wave-particle interactions between chorus waves and electrons. Combining several measurements of at least three energy channels into a full pitch-angle resolution throughout the LEO region, with a time resolution of at least 15 s, will enable research of loss processes from the RBs.

To understand the energy budget of solar eruptions, the second science goal of this mission is to measure solar ENAs. This requires novel observations in an energy range well exceeding the magnetospheric ENA range. For this purpose, we use the geomagnetic field as a filter of solar particles and measure the ENA flux, thus inferring the flux that originates from the solar direction. Solar ENAs can only be measured reliably at energies exceeding the ring-current ion energies.

2.3 Technological objectives

In addition to the science objectives outlined above, FORESAIL-1 has a technological objective to ensure the sustainable use of space and to set a precedent for maintaining clean orbits. The objective is to test the plasma brake technology and achieve at least a 100 km lowering of the spacecraft altitude at mid-to-high altitude LEO. The consequences of this lowering of the orbit are 1) the orbital drift of the mission allowing monitoring the science objectives as a function of MLT, and 2) demonstrating that the technology can be used to de-orbit spacecraft. We will observe efficiency and performance of the plasma brake during the experiment to determine general information about the orbit lowering process. The success of the plasma brake experiment (and thus the completion of the mission's sustainability goals) is dependent on the reliable operation of the avionics, making reliability a primary design driver for FORESAIL-1. Radiation effects are identified as a major potential source of failures, hence radiation hardening techniques are used in the design.

3 Requirements

The study of precipitating electrons from the RBs is intrinsically coupled to the characteristic energy ranges of the electron seed populations there. Scientific and operational requirements are as follows:

1. NOAA/POES, for which the energy resolution is $(E_2 - E_1)/E_1 = 3$ (where E_1 and E_2 are the upper and lower limits for consecutive integral channels), provides the lower reference bar in terms of energy resolution (Evans & Greer, 2006). The nominal energy resolution for FORESAIL-1 is 0.4 between the upper and lower limits of a channel.
2. The particle detector must have a sufficient discriminating ability between electrons and protons, such that the electron channel does not suffer from proton contamination. For lower energy channels there is no contamination, while in the higher energy channels we allow a small background, however, this should be so small that the electrons are discernible.
3. The orbit must drift to cover several MLTs.

- 281 4. For electron precipitation and solar ENA measurements, the orbital altitude should
282 lie between 400 km and 800 km.
- 283 5. The electron pitch angle resolution should include at least three bins measured
284 every 15 s.
- 285 6. The mission profile must allow for the use of the plasma brake for orbital and al-
286 titude control.
- 287 7. The mission profile must provide the ability for daily updates of measurements
288 of orbital parameters to assess the effect of the plasma brake, once activated.

289 In order to achieve the above scientific requirements, the spacecraft spin axis must
290 be oriented with 3° accuracy, with spin of 4.00 ± 0.04 rpm. Attitude determination sys-
291 tem must supply the magnetic field vector with 1° accuracy and the satellite position
292 must be known with 5-km accuracy. There must be a ~ 1 kbs $^{-1}$ data downlink.

293 4 Description of the Mission

294 4.1 General Concept

295 FORESAIL-1 is a nanosatellite mission in LEO designed to answer the science ob-
296 jectives outlined in Section 2. The payload consists of a PArticle Telescope (PATE) and
297 a Plasma Brake (PB). PATE will measure energetic electrons in the energy range 80–
298 800 keV as well as H^+ ions (protons) and neutral atoms in the energy range 0.3–10 MeV.
299 PB consists of a tether that will be used to lower the spacecraft altitude. The spacecraft
300 is constrained under the CubeSat 3U standard to fit the two payloads.

301 4.2 Mission Timeline and Orbit

302 The manufacturing of the FORESAIL-1 payload and spacecraft started in 2018 and
303 the manufacturing and integration will continue throughout 2019 until launch. The space-
304 craft is scheduled to be launched in 2020 into a Sun-synchronous orbit at or lower than
305 700 km altitude. Available launch opportunities are sought in 2019. Following the suc-
306 cessful launch of the mission, the 1-month commissioning phase is scheduled to start im-
307 mediately. After the commissioning phase, the mission's primary science phase is sched-
308 uled for 4 months at the initial Sun-synchronous orbit. After the primary phase, the plasma
309 brake will be applied to lower the spacecraft by more than 100 km such that 1) the plasma
310 braking force is fully demonstrated and 2) from the lowered orbit the spacecraft will nat-
311 urally de-orbit after 25 years. The lowering of the orbit will inject the spacecraft into
312 a drifting polar orbit, allowing precipitation measurements in different MLTs. Follow-
313 ing the successful orbital manoeuvring of the spacecraft, the science phase continues with
314 detecting particle precipitation in the drifting orbit for at least 1–2 years. After this will
315 be the ENA measurement phase. There is a possibility of an extended science phase that
316 will be scheduled depending on the health of the spacecraft.

317 4.3 Spacecraft Conjunctions

318 FORESAIL-1 can be used in conjunction with various other spacecraft in order to
319 determine the origin of precipitating particles observed. Spacecraft that can provide con-
320 text to the FORESAIL-1 observations include the Solar and Heliospheric Observatory
321 (SOHO), STEREO, the Advanced Composition Explorer (ACE), Wind, DSCOVR, the
322 Geostationary Operational Environmental Satellites (GOES), and the Parker Solar Probe.
323 These missions directly monitor solar wind conditions, coronal mass ejections and so-
324 lar energetic particles.

325 The conditions encountered by FORESAIL-1 will depend strongly on the state of
326 the other regions in the magnetosphere. Simultaneous observations from satellites such
327 as Cluster, the Magnetospheric Multi-Scale mission, the Time History of Events and Macroscale

328 Interactions during Substorms spacecraft (THEMIS), and the Geomagnetic Tail Lab (GEO-
329 TAIL) will be invaluable for understanding the global context in which the FORESAIL-
330 1 measurements are made. In particular, when located in the relevant region, these space-
331 craft can monitor substorms occurring in the magnetotail and the associated fast earth-
332 ward plasma flows which are also the sources of the energetic particle precipitations to
333 be measured by FORESAIL-1, in addition to the RB source. They can also provide in-
334 formation about the wave activity in the magnetosphere, which will be key to interpret-
335 ing the FORESAIL-1 observations. In the regions closer to Earth, data from the recently-
336 launched Arase mission in the radiation belts will be of particular importance. Direct
337 complementary observations to FORESAIL-1 will be provided by the POES satellites,
338 which will provide precipitating particle data at similar energy ranges, however these data
339 are often problematic and require corrections.

340 4.4 Coordinated Ground-Based Observations

341 Coordinated observation will also be possible with ground-based instrumentation.
342 Whenever suitable conjunctions with riometer chains such as the Finnish chain operated
343 by Sodankylä Geophysical Observatory or the Canadian chain (NORSTAR) take place,
344 it will be possible to compare energetic particle precipitation patterns to those inferred
345 from cosmic noise absorption measurements. The special case of the Kilpisjärvi Atmo-
346 spheric Imaging Receiver Array (KAIRA) is of particular interest, as this instrument,
347 which may be used as a multibeam, multifrequency riometer could allow to finely study
348 energetic precipitation along the FORESAIL-1 overpass. Indeed, KAIRA can provide
349 1 s time resolution observations of cosmic noise absorption with beams of $10^{\circ}30'$ width,
350 depending on the considered frequency, which is accurate enough to study, e.g., individ-
351 ual patches of pulsating aurora with KAIRA (Grandin et al., 2017), suggesting that it
352 may be possible to study mesoscale (<100 km) structures in energetic precipitation us-
353 ing FORESAIL-1 and KAIRA conjunctions.

354 During conjunctions, it can also prove valuable to combine FORESAIL-1 data with
355 observations of other space weather manifestations. For instance, auroral precipitation
356 can be inferred from observations by all-sky imagers such as the MIRACLE network in
357 Fennoscandia, and the geomagnetic context of FORESAIL-1 measurements can be given
358 more accurately during conjunctions with ground-based magnetometer networks as well
359 as by making use of polar cap convection maps derived from Super Dual Auroral Radar
360 Network observations (SUPERDARN). Finally, FORESAIL-1 precipitation data could
361 prove useful in studies focusing on electron density enhancements in the ionosphere us-
362 ing, e.g., ionosondes or incoherent scatter radars such as the European Incoherent Scatter
363 radars (EISCAT). The latter ones also enable the study of effects such as ionospheric
364 Joule heating or ion outflow, as they measure ion and electron temperatures and ion line-
365 of-sight velocity, and when in a specific configuration they also allow estimating electric
366 fields (Nygrén et al., 2011).

367 5 Payloads

368 The FORESAIL-1 mission will carry two science payloads, the Particle Telescope
369 (PATE) and the Plasma Brake (PB).

370 5.1 Particle Telescope (PATE)

371 PATE measures energetic electrons, H^+ ions (protons) and neutral H atoms. The
372 targeted energy range of hydrogen measurement is 0.3–10 MeV, which covers the en-
373 ergies above the typical ring-current proton energies. This is to avoid the neutral hydro-
374 gen background originating from the interaction of the ring current with the geocorona.
375 The primary energy range for electrons is 80–800 keV. In addition, the instrument is

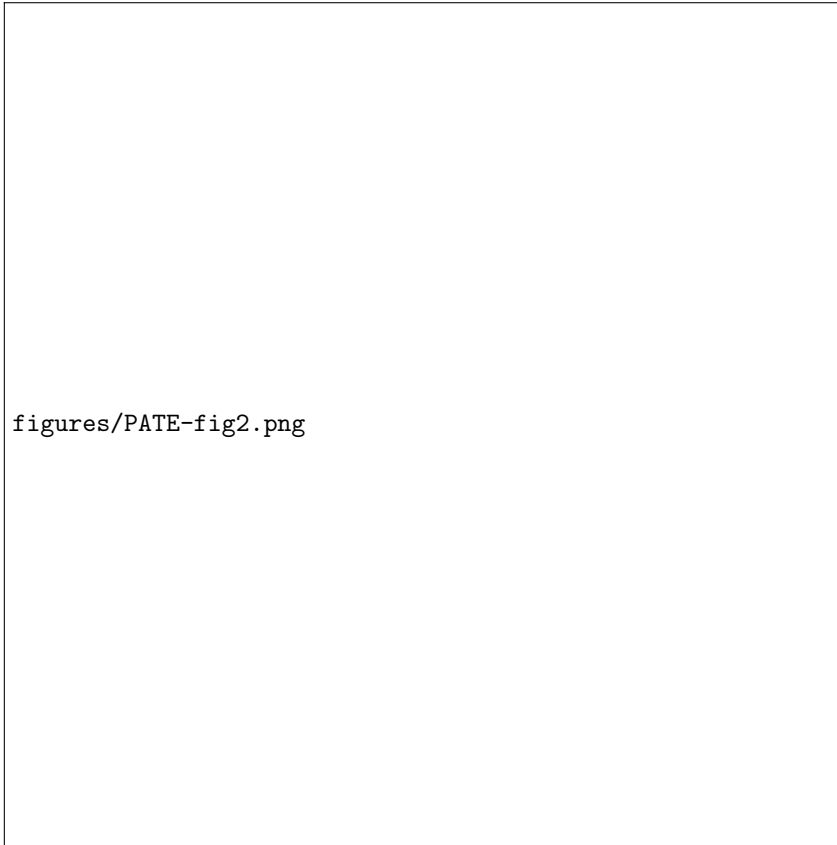


Figure 2. a) Mechanical design concept of PATE. b) Schematic of the anti-coincidence (AC) and main detector (D) stack of each telescope.

376 sensitive to electrons at higher and lower energies in channels, where reliable particle iden-
 377 tification cannot be performed, but especially the high-energy integral channel is still valu-
 378 able since the contamination from heavier species comes only from relativistic protons,
 379 which have low fluxes compared to relativistic electrons in typical conditions.

380 PATE consists of two particle telescopes with identical stacks of detectors (see Fig.
 381 2). The longer Telescope 1 is directed along the long axis of the spacecraft, that is, per-
 382 pendicular to the rotation axis, and thus, it scans the directions in a plane perpendic-
 383 ular to the rotation axis of the spacecraft. The shorter Telescope 2 is directed along the
 384 rotation axis, so it can maintain a stable orientation. When the rotation axis is pointed
 385 towards the Sun, the telescope is able to measure the neutral hydrogen flux from the Sun.
 386 Note that the instrument itself does not determine the hydrogen charge state but relies
 387 on the geomagnetic field as a rigidity filter and on the measurement of angular distri-
 388 bution to disentangle the neutral flux from the solar direction. The motivation for the
 389 use of longer collimator in Telescope 1 is to improve the pitch angle angular resolution
 390 to better than 10 degrees for the scanning telescope.

391 Both telescopes have a mechanical collimator defining the aperture, consisting of
 392 an aluminum tube housing 18 (12) ($500\ \mu\text{m}$ Al + $500\ \mu\text{m}$ Ta) collimator rings in Tele-
 393 scope 1 (Telescope 2), followed by a stack of silicon detectors, D1, D2, and D3, measur-
 394 ing the energy losses of the particles in adjacent layers. The measured signals allow the
 395 determination of particle energy and the identification of particle species (electron / H).
 396 The thicknesses of the D detectors are $20\ \mu\text{m}$, $350\ \mu\text{m}$, and $350\ \mu\text{m}$, respectively. The D1

397 detectors have a bias voltage of 5 V, while the other ones are biased at 70 V. D1 and D2
 398 detectors are segmented so that the central elements have diameters of 5.2 mm while the
 399 total active-area diameters of both are 16.4 mm. D3 has a single active area of 16.4 mm
 400 diameter. Both detector stacks are covered at the bottom of the collimator by two thin
 401 (nominally 0.5 μm each, 1 mm apart) Ni foils preventing low-energy (< 250 keV) ions
 402 and soft (< 500 eV) photons from entering the detector stack. Each aperture is limited
 403 from above by an annular anti-coincidence detector AC1 (300 μm thickness) with a cir-
 404 cular hole of 14.0 mm diameter in the middle and an outer active-area diameter of
 405 33.8 mm. Another single-element circular anti-coincidence detector AC2 (350 μm thick-
 406 ness, 33.8 mm active-area diameter) at the bottom of the stack flags particles penetrat-
 407 ing the whole D detector stack. Note that while the AC2 is operated in anti-coincidence
 408 with the D detectors for the nominal energy range of the instrument (particles stopping
 409 in the D stack), PATE still analyses the D detector pulse heights for particles trigger-
 410 ing AC2 but not AC1 to provide integral flux channels above the nominal energy ranges.
 411 The distances from upper surface to upper surface in the detector stack AC1–D1–D2–
 412 D3–AC2 are 2.5 mm, 2.0 mm, 2.5 mm, and 2.5 mm. The lower Ni foil is 3.2 mm above
 413 the upper surface of AC1.

414 Signal processing is based on continuous sampling and digitization of the analog
 415 signals and on digital filtering and pulse height analysis. The signal processing board con-
 416 tains 16 Analog to Digital Converters (ADCs) and a *Microsemi ProAsic3L* Field Pro-
 417 grammable Gate Array (FPGA) handling the signal processing for both telescopes. The
 418 signal sampling rate in each ADC channel is 10 MHz, and the digital streams are pro-
 419 cessed by the FPGA, which is running at 40 MHz. The logic analyzes the incoming dig-
 420 ital data streams, detects pulses, and identifies the particle for each valid coincidence event,
 421 counting and rejecting from further analysis any events not matching validity criteria.
 422 Valid particle events are then counted in separate counters based on their detection time,
 423 species and measured energy, forming the bulk of the science data of the instrument. The
 424 electron (hydrogen) spectrum consists of seven (ten) energy channels, log-spaced in mea-
 425 sured energy.

426 **5.1.1 Instrument Performance**

427 The performance of the PATE electron measurement has been simulated using GEANT4
 428 (Agostinelli et al., 2003). The simulation is performed for an isotropic electron distri-
 429 bution launched from a (15-cm radius) spherical surface surrounding PATE. The simu-
 430 lated pulse heights of all D-detector signals are analysed to separate electrons and hy-
 431 drogen (ions/ENAs) and to measure particle energies, as in the FPGA-based on-board
 432 analysis. Particles producing a hit (i.e., an energy deposit > 50 keV) only in D2 are iden-
 433 tified as electrons and particles producing a hit only in D1 are identified as hydrogen.
 434 Hit levels can be set freely in the logic, but values lower than 50 keV in D1a, D1c, AC1
 435 and AC2 (see Fig. 2) should not be used as the simulated RMS noise levels in those pads
 436 are around 9–14 keV. While electrons are able to produce hits in D1 as well, there is only
 437 a minor level of electron contamination in the nominal hydrogen energy channels, which
 438 require the energy deposit in D1 to exceed 110 keV. If more than two adjacent D lay-
 439 ers detect a pulse, the Delta E – E method is used for clean species separation. The ge-
 440 ometric factor of the seven electron channels as a function of electron energy for (the shorter)
 441 Telescope 2 is shown in Fig. 3 (Oleynik & Vainio, 2019). The high-energy tails of the
 442 response functions are due to the inevitable scattering of electrons off the detectors and
 443 other structures inside the telescope, which prevents the full energy of the electron to
 444 be absorbed in active detector elements. The internal energy resolution of the instru-
 445 ment is much better for hydrogen than for electrons and the response functions are close
 446 to boxcar type within the nominal energy range.

447 The geometric factors of both telescopes are mostly determined by the uppermost
 448 collimator ring (with an inner diameter of 21.5 mm) and the hole of the AC1 detector

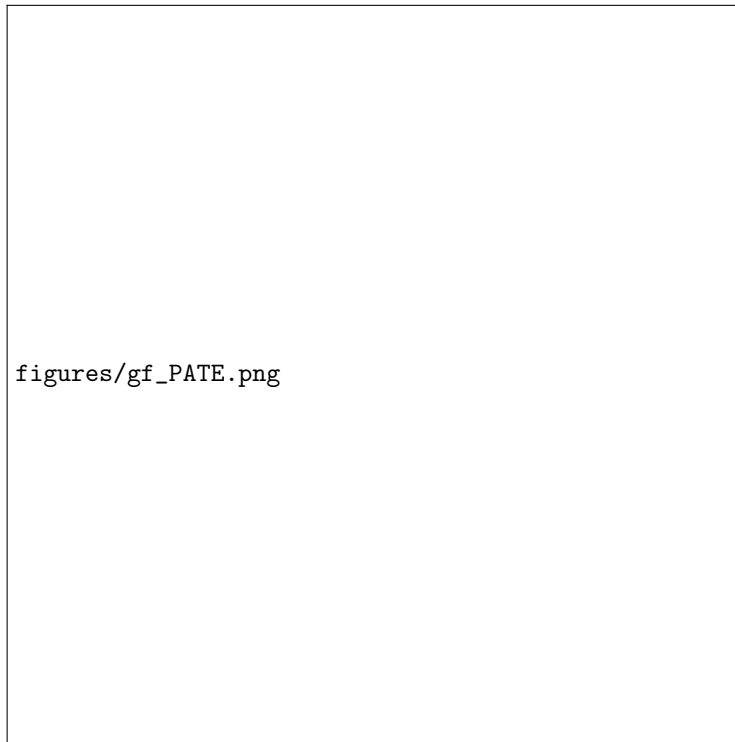


Figure 3. The geometric factor of PATE as a function of energy for the seven electron energy channels within the nominal energy range (80–800 keV), simulated using GEANT4 (Agostinelli et al., 2003). The range above 800 keV is additionally covered by a penetrating particle flux channel.

Data source	Data rate [bit/s]	Data amount per day [kiB]
Rotating telescope	993	10500
Solar pointing telescope	60	633
Housekeeping	13	135
Total	1066	11268

Table 1. Summary of the PATE telemetry budget during science operations.

(diameter of 14 mm), which are at a vertical separation of 12.0 cm (7.0 cm) in Telescope 1 (Telescope 2). The nominal value of the geometric factor is 0.037 cm² sr (0.11 cm² sr) for Telescope 1 (Telescope 2), but especially electrons have somewhat lower values (see Fig. 3) due to scattering off the Ni foils and the D1 detector, causing trajectories to miss the D2 detector. The nominal angular widths of the acceptance cones (half width at half the on-axis value) for the two telescopes are 4.6° and 7.9°, respectively. The instrument can also be operated in a mode where only the central segments of the D1 and D2 are included in the coincidence logic while the rim areas are logically included in the anti-coincidence. This allows to decrease the geometric factors of the telescopes by a factor of about 7. Any detector element can also be switched off from the logic entirely.

5.1.2 Mass, power and telemetry budgets

The mass of PATE is 1.2 kg, consisting of the instrument box and mechanical support structures (435 g), detector and pre-amplified board housings (290 g), the collimators (180 g), cables (115 g), and the rest (180 g), including the back-end electronics stack. The power budget for PATE is 2.5 W, half of which is consumed by the FPGA, with an additional margin of 20%, mainly required to account for the final FPGA power consumption.

The telemetry budget of PATE is summarized in Table 1. Spectral resolution of the data products for both electrons and hydrogen is on average $\Delta E/E \approx 40\%$ within the nominal energy ranges, which means that the spectral counter data consists of eight (ten) differential and one (two) integral channels for electrons (hydrogen). The rotation period, nominally 15 s, of the satellite equals the time resolution of the instrument. This main time frame is further broken in 36 angular sectors for the rotating telescope to provide the angular distribution measurement. Both telescopes deliver, in addition to the spectral counter data, also pulse height data samples, which allow an accurate in-flight calibration and health monitoring of the detection system.

5.2 Plasma Brake (PB)

5.2.1 Operating Principle

The Plasma Brake instrument is designed to measure the Coulomb drag, i.e., the braking force caused by the ionospheric plasma ram flow to an electrically charged tether (Figure 4). When interacting with the surrounding plasma, the negative tether gathers positive ions, which tends to neutralize the tether. To maintain the charge, the tether is connected by a high-voltage power system to a conducting surface (deployable booms for FORESAIL-1) that acts as an electron sink to close the current system through the plasma (Janhunen, 2011). The braking force can be measured in two modes. One is to monitor the system spin rate while charging the tether synchronously with the tether rotation (PB Measurement). The other is to maintain a constant charging and monitor the spacecraft velocity and orbital elements (PB Mode).

figures/PB_operating.png

Figure 4. Operating principle of the PB: an electric current system and a net thrust exerted on the negative tether by the plasma ram flow.

We employ -1 kV voltage, which is the maximum without risking electron field emission from micrometeoroid-struck parts of the tether wires. At this voltage, the expected nominal plasma brake thrust per tether length is 58 nN/m when the tether is perpendicular to the ram flow. This value is obtained by using Equation 1 of Janhunen (2014) and assuming plasma density of $3 \cdot 10^{10} \text{ m}^{-3}$, mean ion mass of 10 proton masses, ram flow speed of 7.8 km/s and tether's effective electric radius of 1 mm. The tether's collected ion current is small, nominally $30 \mu\text{A}$ for a 300 m long tether.

5.2.2 Design

The tether is deployed from a chamber (blue) by the centrifugal force affecting the tether tip mass (gray button inside the red collar) (Figure 5). The mechanical interface through the satellite side panel is provided by an anti-static collar (red) to avoid triple junctions of plasma, insulator, and high voltage tether. The tip mass is locked during the launch by two launch locks located on opposite sides of the tether chamber opening. The tether reel (dark gray) and the stepper motor that turns it (orange) are nested

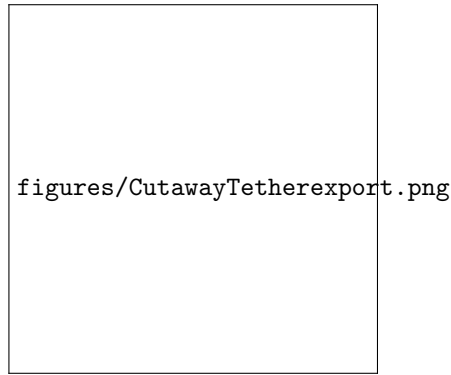


Figure 5. PB payload structure.

501 inside the tether chamber. The tether high-voltage contact is through the conducting
 502 reel and the slider (copper brown) attached straight to the high-voltage converter (or-
 503 ange) board behind the tether chamber.

504 The PB tether is made of thin metallic wires that are periodically bonded to each
 505 to withstand the micrometeoroid and space debris collisions (e.g., Seppänen et al., 2011).
 506 The single wire thickness is a few tens of micrometers to minimise the ion current to the
 507 tether and thus the mass of the power system and size of the electron gathering surface.

508 The nominal FORESAIL-1 tether length is 300 meters requiring ~ 20 Nms of the
 509 total angular momentum to deploy it. The initial angular speed of $180^\circ/\text{s}$ is sufficient
 510 to provide a centrifugal force of 0.4 cN which would safely pull out a tip mass weighing
 511 2.5 g without breaking the tether. The angular momentum is provided by several con-
 512 secutive satellite spin-up and reel-out maneuvers to compensate for the decreasing spin
 513 rate associated with the increasing moment of inertia. Since magnetorquers are used for
 514 attitude control, the angular acceleration is low to avoid the tether winding around the
 515 satellite. It also indicates that a considerable amount of time is needed to provide the
 516 angular momentum. However, after measuring the Coulomb drag force with a few tens
 517 of meters of the tether, the force can be used to spin up the satellite by modulating the
 518 tether voltage in synchronization with the rotation (charging downstream to increase the
 519 spin rate). After deploying the tether and taking PB measurements, the PB mode will
 520 start by continuously charging the tether which in turn will lower the orbit and start the
 521 satellite drift in MLT. When reaching ~ 600 -km altitude and gaining a sufficient drift in
 522 MLT, the satellite will be prepared for PATE observations – the tether will be discarded
 523 to allow the spin axis being pointed towards the Sun. It can be done by attempting to
 524 reel in the tether which might break because it would be partially broken by microm-
 525 eteoroids. A broken tether would deorbit in a few months thanks to its large area/mass
 526 ratio. If the tether does not break, the attitude control system and/or PB itself will have
 527 to provide an angular momentum to compensate for an increasing spin rate.

528 **5.2.3 Mass, Power and Telemetry Budgets**

529 The mass of the PB is 0.6 kg including a margin of 25%. The structure (frame, tether
 530 chamber, and motor mounting shaft) contributes 67% to the mass budget. The size of
 531 the system is $67 \times 84 \times 96$ mm. For the two measurement modes of the PB, the power bud-
 532 get for PB is 600 mW. For the tether reeling, the motor and the controller consumes 7
 533 W continuously. In case the reel-out power cannot be provided continuously by the space-
 534 craft, the operation can be done in stages. The telemetry budget of the PB is summarised
 535 in Table 2. To reduce the overall telemetry budget, the long-duration routine PB mode

Mode	Data rate [bit/s]	Data amount per day [kiB]
Reel-Out/In	128	1350
PB Mode	19	200
PB Measurement	256	2700
Standby	64	675

Table 2. Summary of the PB telemetry budget for the operation modes.

Subsystem	Planned mass (g)	Mass with contingency (g)	Fraction (%)
OBC	80	96	2
EPS	926	1093	23
Magnetorquers	240	288	6
UHF Transceiver	80	96	2
Antennas	50	60	1
Structure	1033	1240	26
PATE	1000	1200	26
PB	600	660	14
Total	4009	4733	100

Table 3. FORESAIL-1 mass budget.

536 uses a lower telemetry rate. Frequent housekeeping data are not required because in the
 537 PB mode, altitude change over weeks to months will show the success of experiment.

538 6 Spacecraft platform

539 The platform has been designed to accommodate the payloads and to provide data,
 540 power and mechanical interfaces. The overall mission tree for the FORESAIL-1 is pre-
 541 sented in Figure 6. Since one of the key technological drivers for the mission is reliabil-
 542 ity, the avionics stack has several designs to this end. The avionics stack is enclosed in
 543 a vault providing substantially better shielding than what is typically seen on CubeSats
 544 (around 4 mm equivalent aluminium, instead of the more typical 2 mm), thus enhanc-
 545 ing system tolerance to total dose. Single-event effects will be mitigated using dual cold
 546 redundancy, hardware overcurrent protection, minimization of the software footprint, and
 547 systematic data integrity checks. Finally, the FORESAIL-1 components will be submit-
 548 ted to radiation test campaigns; the radiation response data will be made available pub-
 549 licly in order to benefit from the broader field of (small) satellite technology and help
 550 other designers addressing this issue.

551 The avionics stack consists of the Electrical Power System (EPS) for power collec-
 552 tion, storage and distribution, Communication System for telemetry, On-Board Com-
 553 puter (OBC) for telemetry handling and mission and payload management and data stor-
 554 age, and Attitude Determination and Control System (ADCS) for maintaining the atti-
 555 tude modes during different operation phases. The mechanical structure satisfies di-
 556 mensional limitations of the CubeSat standard and ensures modular configuration of the
 557 spacecraft's subsystems. The configuration of the platform is shown in Figure 7. The to-
 558 tal mass budget is shown in Table 3.



Figure 6. FORESAIL-1 mission product tree.



Figure 7. Spacecraft structure including the subsystems without shielding.

Parameter	X,Y axes	Z axis
Number of wire turns	184	952
Nominal current, mA	26.2	19.3
Dipole moment, Am ²	0.2	0.2
Power, mW	51.7	56.5

Table 4. Quantitative parameters for the air core magnetorquers.

6.1 Platform subsystems

Each payload has different requirements for attitude. PATE needs to be oriented towards the Sun, while the detector with longer collimator scans the environment in the directions perpendicular to the Earth–Sun vector. The PB needs the spinning control for deploying and maintaining the tension of the tether. While the PB does not need specific pointing direction, its tether deployment introduces a mass distribution change that will require a proper control of the spacecraft angular momentum.

The attitude determination and control system (ADCS) is divided into Attitude Determination System (ADS) and Attitude Control System (ACS). The ADS is equipped with gyroscope (L3GD20H), magnetometer (LIS3MDL), and in-house built sun sensors (Noman et al., 2017). The angular velocity of the spacecraft is a crucial parameter for the payload attitude modes, thus gyroscope is necessary. Sun sensors are required for a precise sun pointing control, and magnetometers are needed for properly using with attitude control. The outputs will provide a full attitude information through using an unscented Kalman filter algorithm on all sensors.

The ACS changes the orientation of the spacecraft by using magnetorquers. There is a closed loop feedback, which ensures the maintenance of desired attitude by repeating the torque command until the desired orientation is achieved. The mission requirements for PATE and PB impose specific constraints on the attitude control. The spacecraft uses the following attitude control modes:

- Detumble mode: To stabilize the spacecraft after deployment
- Spin control mode: In order to deploy the PB tether, this mode spins up the spacecraft preferably with the spin axis being aligned with the earth pole. After deorbiting, spin down might be required during tether reel in if the tether does not break.
- Sun pointing mode: This mode continuously points Telescope 2 (at $-Y$ axis) towards the sun while spinning in order for Telescope 1 (at Z -axis) to scan the sky.

Magnetorquers are sufficient to provide all necessary control modes for the manipulation of the attitude and angular velocity. They are designed in-house, in form of air coils, so that they can be integrated to the solar panels (for the X and Y axes), and on a small factor magnetorquer driver board for the Z axis. All axes have two magnetorquers connected in parallel. The designed magnetorquers are driven through a custom-built coil driver to optimize either consumed power or the generated magnetic moment. The quantitative parameters of air core magnetorquers are given in Table 4.

The EPS of the satellite consist of solar panels, power conditioning and power distribution (Ali et al., 2014), (Mughal et al., 2014). The solar panels are mounted on every long side of the satellite. The solar panels at other sides than where PATE is located consist of 7 solar cells connected in series, whereas the panel at the PATE side consists

of 6 cells in order to provide space for the telescope. The power conditioning consists of switching buck converters to convert the incoming solar power to the battery voltage level. A perturb and observe based algorithm extracts the maximum power from the solar cells. Each subsystem houses a linear regulator to effectively convert the voltage down to a stable 3.3 V with a low ripple factor. The theoretical efficiency of the EPS is above 85 %. All losses have been accounted for in the calculation of power budget. The maximum input power is 7 W, whereas the average power consumption in the nominal mode 3.7 W.

The on-board computer (OBC) is the satellite's main computer responsible for computational and data storage needs, running the ADCS algorithms, and storing the telemetry and housekeeping data logs. A safety-critical ARM Cortex-R4 based processor is selected as the central OBC of the spacecraft. The processor features 256 k data rapid-access memory and 3 MB of program flash. There are external flash memory devices also interfaced with the processor. To facilitate possible faults due to radiation, the OBC houses two cold redundant symmetric processors. Only one of the processors is active and powered. The arbiter switches the control to the redundant processor in case of failure. The OBC is responsible for operational work during the PB and PATE operations and collects all relevant telemetry data for downlink.

The UHF transceiver onboard the FORESAIL-1 consist of CC1125 transceiver with maximum output power of 15 dBm (30 mW); an external power amplifier RF5110G (gain: 31.5 dB, maximum output power 34.5 dBm) to amplify the power to desired 1.5-watt power in the transmit chain. In the receive chain, it consist of a Low Noise Amplifier and a bandpass filter.

7 Ground Segment and Operations

The primary ground station used for satellite operation is located in Aalto University Campus in Espoo, Finland. The ground station operates mainly as a radio amateur satellite station and has capabilities for operation on radio amateur UHF, VHF and S-bands. Due to its northern location the ground station has an average link time to polar orbit up to 90 minutes per day for all passes above the horizon. Ground station radio systems are built based on the Software Defined Radio (SDR) architecture which facilitates easy satellite-specific customization. The ground station infrastructure and equipment are designed and operated by students and serve also for educational purposes for the Aalto University. The Aalto University ground station also operates as the mission control centre.

Typically, each satellite pass provides 10-20 min of link time between satellite and ground station. The data rate requirements for FORESAIL-1 in science mode require the downlink data rate to be approximately 8 kbps. Since the data rate requirements are not stringent in order to accomplish both the missions, the ground station at Aalto University easily handles the data rate requirements.

8 Data Products

FORESAIL-1 data products are outlined in Table 5. The Aalto University ground station is responsible for downlinking the L0/L1 data containing general spacecraft housekeeping data, PATE raw data, PB housekeeping and mission log information. These low level data products are shared forward using file-based web interface. For PATE data processing, Level 1 raw data files combined to ADCS metadata and orbital information are used to produce calibrated and geolocated measurements of the particle fluxes.

These data products will be used to demonstrate that the PB de-orbits the satellite at a measurable amount, as a function of time. The PATE data will be used to in-

Provider	Data product	Details
Mission	List of data availability	
Spacecraft	Orbital data, Attitude	Includes position and altitude required to estimate the PB performance
PB	Electric current in the tether L0 telemetry stream L1 raw data L2 calibrated data L3 derived products	Plasma density L2 and plasma density including position
PATE	Flux L0 telemetry stream L1 raw data L2 calibrated data (fluxes) L3 derived products	L2 including location Precipitation maps (varying time resolutions) Angular distribution data (spin resolution) Event catalogues (mission duration)

Table 5. FORESAIL-1 data products. PATE fluxes are given as function of energy, time and pointing azimuth.

644 fer the precipitation energy spectrum in time and place, addressing the science objec-
645 tives. The science data are open for everyone, with the nominal rules-of-the-road typ-
646 ical in the field of space physics.

647 9 Summary and Discussion

648 The increasing number of small satellites launched into Earth’s orbit raises timely
649 concerns about the sustainable use of space. Small, rapidly built and launched satellites
650 have a large future potential for scientific and commercial use. However, the satellites
651 will become debris sooner rather than later, if they have poor radiation tolerance and
652 if they are not de-orbited at the end of mission. The Finnish centre Of excellence in RE-
653 search of SustAINable space (FORESAIL) funded by the Academy of Finland tackles
654 this issue by focusing both on science of the near-Earth radiation environment and on
655 novel technological solutions related to building more resilient instruments and debris
656 removal.

657 The first nanosatellite designed and built by the Centre of Excellence, FORESAIL-
658 1, is a 3U cubesat operating at polar LEO orbit at and below 700 km which will pro-
659 duce energy-dependent pitch angle spectra of electrons and protons that precipitate from
660 the RBs into the ionosphere. Further, it will measure energetic neutral atoms (ENAs)
661 from the Sun and test the PB technology to lower the spacecraft altitude and manage
662 its orbit in space.

663 Today, nanosatellites can address significant scientific questions. This requires fo-
664 cused measurements and innovative technological approaches, as well as coordination with
665 the other spacecraft and facilities operating simultaneously. The FORESAIL-1 PATE
666 instrument will make unprecedented and precise measurements of precipitating electrons
667 and protons with high temporal resolution. It will be able to discriminate between elec-
668 trons and protons, over a wide energy range (80 – 800 keV for electrons and 0.3 – 10 MeV
669 for protons and neutral atoms). The large coverage of the polar cap at different orbital
670 planes is achieved by operating the PB at the beginning of the mission, which sets the

671 spacecraft orbital plane to drift in magnetic local time. This is the first time such a ma-
672 noeuvre is attempted with a nanosatellite, and if successful, it will open new avenues for
673 controlling the orbits of propellantless spacecraft, expanding their operational and ob-
674 servational ranges.

675 FORESAIL-1 is targeted to make important advances in radiation belt physics. With
676 simultaneous observations in the solar wind, magnetosphere and from the ground, FORESAIL-
677 1 will allow quantifying the role of solar wind and outer magnetospheric driving, and the
678 role of different plasma waves in the inner magnetosphere in the precipitation process.
679 The primary science phase allows connecting precipitation signatures and mechanisms
680 to geomagnetic activity levels and solar wind conditions. Together with the novel Vlasi-
681 ator model, a global hybrid-Vlasov simulation (Palmroth et al., 2018), it will be possi-
682 ble to tie precipitation measurements to global processes in the outer magnetosphere for
683 the first time, as Vlasiator begins its full six-dimensional operation before the launch of
684 FORESAIL-1. The six dimensions refer to three dimensions in the ordinary space and
685 three in the velocity space to describe the full particle distribution function, which is used
686 to infer the energy spectrum and pitch angle in time. At the time of writing, Vlasiator
687 allows already 2D electron precipitation calculations (see Fig. 1), which are in reason-
688 able agreement with previous estimates (Hardy et al., 1985). Once the model is fully 6D,
689 *in situ* observations of electron precipitation can be directly compared to kinetic pro-
690 cesses anywhere in the magnetosphere, without limitations as to whether a spacecraft
691 traverses particular regions. This unprecedented plan will likely open new avenues in space
692 physics.

693 Successful observations of ENAs from the Sun will allow estimating for the first time
694 comprehensively estimating the suprathermal coronal ion population indirectly. This is
695 the key knowledge for improved understanding of the charged particle acceleration pro-
696 cesses at the CME-driven shock waves close to the Sun and of the CME energy budget.
697 The solar ENA flux has been measured only once in a very fortuitous event (Mewaldt
698 et al., 2009). Observing the ENA flux from the Sun on a regular basis as a function of
699 time and solar activity is unprecedented.

700 The demonstration of the altitude manoeuvre of FORESAIL-1 will bring poten-
701 tial for future applications for the PB as a standard tool for removing satellites from their
702 orbits. This is in particular a compelling solution considering the possibly upcoming reg-
703 ulations for including debris mitigation techniques in newly launched spacecraft.

704 FORESAIL-1 is at the forefront of scientific nanosatellites. The advances we have
705 made will be particularly important in demonstrating the usefulness of nanosatellites in
706 making relevant physics and discovery measurements (ENA), whose spatio-temporal res-
707 olution could be brought to a new level using fleets of nanosatellites. Technological so-
708 lutions of FORESAIL-1 have particularly far reaching impact for future debris removal
709 solutions and orbit control. All these aspects are expected to pave the way for the sus-
710 tainable use of space.

711 Acknowledgments

712 The Finnish Centre of Excellence in Research of Sustainable Space, building and launch-
713 ing three FORESAIL missions is funded through the Academy of Finland with grant num-
714 bers 312351, 312390, 312358, 312357, and 312356.

715 We acknowledge The European Research Council for Starting grant 200141-QuESpace,
716 with which Vlasiator was developed, and Consolidator grant 682068-PRESTISSIMO awarded
717 to further develop Vlasiator and use it for scientific investigations. We gratefully also
718 acknowledge the Academy of Finland (grant numbers 138599, 267144, 309937, and 309939).
719 We acknowledge the CSC – IT Center for Science Grand Challenge grant for 2018, with
720 which the Vlasiator simulation run was carried out. Vlasiator (<http://www.physics.helsinki.fi/vlasiator/>,

(Palmroth, 2019)) is distributed under the GPL-2 open source license at <https://github.com/fmihpc/vlasiator/> (Palmroth & the Vlasiator team, 2019). Vlasiator uses a data structure developed in-house (Sandroos, 2019), which is compatible with the VisIt visualization software (Childs et al., 2012) using a plugin available at the VLSV repository. The Analysator software (<https://github.com/fmihpc/analysator/>, (Hannuksela & the Vlasiator team, 2019) was used to produce the presented figures. The run described here takes several terabytes of disk space and is kept in storage maintained within the CSC IT Center for Science. Data presented in this paper can be accessed by following the data policy on the Vlasiator web site.

References

- Agostinelli, S., Allison, J., Amako, K., Apostolakis, J., Araujo, H., Arce, P., . . . G EANT4 Collaboration (2003, July). GEANT4—a simulation toolkit. *Nuclear Instruments and Methods in Physics Research A*, *506*, 250–303. doi: 10.1016/S0168-9002(03)01368-8
- Ali, A., Mughal, M., Ali, H., & Reyneri, L. (2014). Innovative power management, attitude determination and control tile for cubesat standard nanosatellites. *Acta Astronautica*, *96*, 116 - 127. Retrieved from <http://www.sciencedirect.com/science/article/pii/S0094576513004165> doi: <https://doi.org/10.1016/j.actaastro.2013.11.013>
- Asikainen, T., & Mursula, K. (2013, October). Correcting the NOAA/MEPED energetic electron fluxes for detector efficiency and proton contamination. *J. Geophys. Res. Space Physics*, *118*, 6500–6510. doi: 10.1002/jgra.50584
- Baker, D. N., & Kanekal, S. G. (2008, February). Solar cycle changes, geomagnetic variations, and energetic particle properties in the inner magnetosphere. *Journal of Atmospheric and Solar-Terrestrial Physics*, *70*, 195-206. doi: 10.1016/j.jastp.2007.08.031
- Barcus, J. R., Brown, R. R., Karas, R. H., Brønstad, K., Trefall, H., Kodama, M., & Rosenberg, T. J. (1973, March). Balloon observations of auroral-zone X-rays in conjugate regions. *Journal of Atmospheric and Terrestrial Physics*, *35*, 497-511. doi: 10.1016/0021-9169(73)90039-1
- Barthelemy, M., Vladimir, K., Anne, V., Frédéric, R., Sebastien, P., & Laurence, C. (2018, April). AMICal and ATISE : two cubesats optical payload for space weather monitoring. In *Egu general assembly conference abstracts* (Vol. 20, p. 10580).
- Bastida Virgili, B., Dolado, J. C., Lewis, H. G., Radtke, J., Krag, H., Revelin, B., . . . Metz, M. (2016, September). Risk to space sustainability from large constellations of satellites. *Acta Astronautica*, *126*, 154-162. doi: 10.1016/j.actaastro.2016.03.034
- Bekey, I. (1997). Project Orion: Orbital Debris Removal Using Ground-Based Sensors and Lasers. In B. Kaldeich-Schuermann (Ed.), *Second european conference on space debris* (Vol. 393, p. 699).
- Bonnal, C., Ruault, J.-M., & Desjean, M.-C. (2013, April). Active debris removal: Recent progress and current trends. *Acta Astronautica*, *85*, 51-60. doi: 10.1016/j.actaastro.2012.11.009
- Bradley, A. M., & Wein, L. M. (2009). Space debris: Assessing risk and responsibility. *Advances in Space Research*, *43*(9), 1372 - 1390. doi: 10.1016/j.asr.2009.02.006
- Campbell, J. W. (2000, December). *Using lasers in space: Laser orbital debris removal and asteroid deflection* (Occasional Paper No. 20). Maxwell Air Force Base, Alabama: Air University.
- Chen, Y., Reeves, G. D., & Friedel, R. H. W. (2007, September). The energization of relativistic electrons in the outer Van Allen radiation belt. *Nature Physics*, *3*,

- 614-617. doi: 10.1038/nphys655
- 773 Childs, H., Brugger, E., Whitlock, B., Meredith, J., Ahern, S., Pugmire, D., ...
 774 Navr'atil, P. (2012, Oct). VisIt: An End-User Tool For Visualizing and Analyzing
 775 Very Large Data. In *High Performance Visualization—Enabling Extreme-Scale*
 776 *Scientific Insight* (p. 357-372). Chapman & Hall / CRC.
- 777 Crew, A. B., Spence, H. E., Blake, J. B., Klumpar, D. M., Larsen, B. A., O'Brien,
 778 T. P., ... Widholm, M. (2016). First multipoint in situ observations of electron
 779 microbursts: Initial results from the nsf firebird ii mission. *Journal of Geophysical*
 780 *Research: Space Physics*, *121*(6), 5272-5283. doi: 10.1002/2016JA022485
- 781 Elkington, S. R., Hudson, M. K., & Chan, A. A. (2003, March). Resonant
 782 acceleration and diffusion of outer zone electrons in an asymmetric geomag-
 783 netic field. *Journal of Geophysical Research (Space Physics)*, *108*, 1116. doi:
 784 10.1029/2001JA009202
- 785 Emslie, A. G., Kucharek, H., Dennis, B. R., Gopalswamy, N., Holman, G. D., Share,
 786 G. H., ... Zurbuchen, T. H. (2004, October). Energy partition in two solar
 787 flare/CME events. *Journal of Geophysical Research (Space Physics)*, *109*, A10104.
 788 doi: 10.1029/2004JA010571
- 789 European Space Agency. (2014). Space debris mitigation policy for agency projects.
 790 reference ESA/ADMIN/IPOL(2014)2 and annexes [Computer software manual].
- 791 Evans, & Greer. (2006). *Sem-2 documentation for noaa-15 and later satellites,*
 792 *version 2v2.0, rev 2006.* [https://ngdc.noaa.gov/stp/satellite/poes/](https://ngdc.noaa.gov/stp/satellite/poes/documentation.html)
 793 [documentation.html](https://ngdc.noaa.gov/stp/satellite/poes/documentation.html). (Accessed: 2018-11-23)
- 794 Evans, D. S., & Greer, M. S. (2000). *Polar orbiting environmental satellite space*
 795 *environment monitor-2: Instrument description and archive data documentation.*
 796 US Department of Commerce, National Oceanic and Atmospheric Administration,
 797 Oceanic and Atmospheric Research Laboratories, Space Environment Center.
- 798 for Standardization, I. O. (2011). Space systems – space debris mitigation require-
 799 ments [Computer software manual].
- 800 Graf, K. L., Inan, U. S., Piddychiy, D., Kulkarni, P., Parrot, M., & Sauvaud, J. A.
 801 (2009, July). DEMETER observations of transmitter-induced precipitation of
 802 inner radiation belt electrons. *Journal of Geophysical Research (Space Physics)*,
 803 *114*, A07205. doi: 10.1029/2008JA013949
- 804 Grandin, M., Kero, A., Partamies, N., McKay, D., Whiter, D., Kozlovsky, A., &
 805 Miyoshi, Y. (2017, Jun). Observation of pulsating aurora signatures in cos-
 806 mic noise absorption data. *Geophysical Research Letters*, *44*, 5292-5300. doi:
 807 10.1002/2017GL073901
- 808 Hannuksela, O., & the Vlasiator team. (2019). *Analysator: python analysis toolkit.*
 809 Github repository. Retrieved from <https://github.com/fmihpc/analysator/>
 810 (last access: 09.05.2019)
- 811 Hardy, D. A., Gussenhoven, M. S., & Holeman, E. (1985). A statistical model of au-
 812 roral electron precipitation. *Journal of Geophysical Research*, *90*, 4229-4248. doi:
 813 10.1029/JA090iA05p04229
- 814 Hargreaves, J. K. (1969). Auroral absorption of HF radio waves in the ionosphere:
 815 A review of results from the first decade of riometry. *IEEE Proceedings*, *57*, 1348–
 816 1373. doi: 10.1109/PROC.1969.7275
- 817 Janhunen, P. (2004). Electric sail for spacecraft propulsion. *Journal of Propulsion*
 818 *and Power*, *20*(4), 763-764. doi: 10.2514/1.8580
- 819 Janhunen, P. (2011, March). Electrostatic plasma brake for deorbiting a satellite. *J.*
 820 *Prop. Power*, *26*, 370-372. doi: 10.2514/1.47537
- 821 Janhunen, P. (2014). Simulation study of the plasma-brake effect. *Ann. Geophys.*,
 822 *32*, 1207-1216. doi: 10.5194/angeo-32-1207-2014
- 823 Kennel, C. F., & Petschek, H. E. (1966, January). Limit on Stably Trapped Particle
 824 Fluxes. *Journal of Geophysical Research*, *71*, 1. doi: 10.1029/JZ071i001p00001
- 825 Kero, A., Vierinen, J., McKay-Bukowski, D., Enell, C.-F., Sinor, M., Roininen, L., &
 826

- 827 Ogawa, Y. (2014, August). Ionospheric electron density profiles inverted from a
828 spectral riometer measurement. *Geophysical Research Letters*, *41*, 5370-5375. doi:
829 10.1002/2014GL060986
- 830 Kessler, D. J., & Cour-Palais, B. G. (n.d.). Collision frequency of artificial satellites:
831 The creation of a debris belt. *Journal of Geophysical Research: Space Physics*,
832 *83*(A6), 2637-2646. doi: 10.1029/JA083iA06p02637
- 833 Kim, H.-J., & Chan, A. A. (1997, September). Fully adiabatic changes in storm time
834 relativistic electron fluxes. *Journal of Geophysical Research: Space Physics*, *102*,
835 22107-22116. doi: 10.1029/97JA01814
- 836 Klinkrad, H. (1993, August). Collision risk analysis for low Earth orbits. *Advances*
837 *in Space Research*, *13*, 177-186. doi: 10.1016/0273-1177(93)90588-3
- 838 Kohnert, R., Palo, S., & Li, X. (2011). Small space weather research mis-
839 sion designed fully by students. *Space Weather*, *9*(4). Retrieved from
840 <https://agupubs.onlinelibrary.wiley.com/doi/abs/10.1029/2011SW000668>
841 doi: 10.1029/2011SW000668
- 842 Lappas, V., Adeli, N., Visagie, L., Fernandez, J., Theodorou, T., Steyn, W., &
843 Perren, M. (2011, December). CubeSail: A low cost CubeSat based solar
844 sail demonstration mission. *Advances in Space Research*, *48*, 1890-1901. doi:
845 10.1016/j.asr.2011.05.033
- 846 Li, X., Baker, D. N., Kanekal, S. G., Looper, M., & Temerin, M. (2001). Long term
847 measurements of radiation belts by SAMPEX and their variations. *Geophysical*
848 *Research Letters*, *28*, 3827-3830. doi: 10.1029/2001GL013586
- 849 Li, X., Baker, D. N., Temerin, M., Larson, D., Lin, R. P., Reeves, G. D., ...
850 Mewaldt, R. A. (1997). Are energetic electrons in the solar wind the source
851 of the outer radiation belt? *Geophysical Research Letters*, *24*, 923-926. doi:
852 10.1029/97GL00543
- 853 Mann, I. R., Ozeke, L. G., Murphy, K. R., Claudepierre, S. G., Turner, D. L., Baker,
854 D. N., ... Honary, F. (2016, October). Explaining the dynamics of the ultra-
855 relativistic third Van Allen radiation belt. *Nature Physics*, *12*, 978-983. doi:
856 10.1038/nphys3799
- 857 Marchaudon, A., & Bletly, P.-L. (2015). A new interhemispheric 16-moment model
858 of the plasmasphere-ionosphere system: IPIM. *J. Geophys. Res. Space Physics*,
859 *120*, 5728-5745. doi: 10.1002/2015JA021193
- 860 Matsumura, C., Miyoshi, Y., Seki, K., Saito, S., Angelopoulos, V., & Koller, J.
861 (2011, June). Outer radiation belt boundary location relative to the magne-
862 topause: Implications for magnetopause shadowing. *Journal of Geophysical Re-*
863 *search (Space Physics)*, *116*, A06212. doi: 10.1029/2011JA016575
- 864 McDiarmid, I. B., Burrows, J. R., & Budzinski, E. E. (1975). Average characteristics
865 of magnetospheric electrons (150 eV to 200 keV) at 1400 km. *Journal of Geophys-*
866 *ical Research*, *80*, 73. doi: 10.1029/JA080i001p00073
- 867 McIlwain, C. E. (1966, August). Ring current effects on trapped parti-
868 cles. *Journal of Geophysical Research: Space Physics*, *71*, 3623-3628. doi:
869 10.1029/JZ071i015p03623
- 870 McKay-Bukowski, D., Vierinen, J., Virtanen, I. I., Fallows, R., Postila, M., Ulich, T.,
871 ... Turunen, E. (2015, March). KAIRA: The Kilpisjärvi Atmospheric Imaging
872 Receiver Array—System Overview and First Results. *IEEE Transactions on Geo-*
873 *science and Remote Sensing*, *53*, 1440-1451. doi: 10.1109/TGRS.2014.2342252
- 874 Mewaldt, R. A., Leske, R. A., Stone, E. C., Barghouty, A. F., Labrador, A. W., Co-
875 hen, C. M. S., ... Wiedenbeck, M. E. (2009, March). STEREO Observations of
876 Energetic Neutral Hydrogen Atoms During the 2006 December 5 Solar Flare. *The*
877 *Astrophysical Journal*, *693*, L11-L15. doi: 10.1088/0004-637X/693/1/L11
- 878 Millan, R. M., & the BARREL Team. (2011, July). Understanding relativistic elec-
879 tron losses with BARREL. *Journal of Atmospheric and Solar-Terrestrial Physics*,
880 *73*, 1425-1434. doi: 10.1016/j.jastp.2011.01.006

- 881 Millan, R. M., & Thorne, R. M. (2007, March). Review of radiation belt relativistic
882 electron losses. *Journal of Atmospheric and Solar-Terrestrial Physics*, *69*, 362-
883 377. doi: 10.1016/j.jastp.2006.06.019
- 884 Miyoshi, Y., Oyama, S., Saito, S., Kurita, S., Fujiwara, H., Kataoka, R., ...
885 Tsuchiya, F. (2015, April). Energetic electron precipitation associated with pul-
886 sating aurora: EISCAT and Van Allen Probe observations. *Journal of Geophysical*
887 *Research (Space Physics)*, *120*, 2754-2766. doi: 10.1002/2014JA020690
- 888 Mughal, M. R., Ali, A., & Reyneri, L. M. (2014). Plug-and-play design approach
889 to smart harness for modular small satellites. *Acta Astronautica*, *94*(2), 754 -
890 764. Retrieved from [http://www.sciencedirect.com/science/article/pii/](http://www.sciencedirect.com/science/article/pii/S009457651300369X)
891 [S009457651300369X](http://www.sciencedirect.com/science/article/pii/S009457651300369X) doi: <https://doi.org/10.1016/j.actaastro.2013.09.015>
- 892 Nakamura, R., Isowa, M., Kamide, Y., Baker, D. N., Blake, J. B., & Looper, M.
893 (2000, July). SAMPEX observations of precipitation bursts in the outer radiation
894 belt. *Journal of Geophysical Research: Space Physics*, *105*, 15875-15886. doi:
895 10.1029/2000JA900018
- 896 Noman, M., Zulqamain, S. M., Mughal, M. R., Ali, A., & Reyneri, L. M. (2017,
897 June). Component selection for magnetic attitude subsystem of pnss-1 small satel-
898 lite. In *2017 8th international conference on recent advances in space technologies*
899 *(rast)* (p. 361-367). doi: 10.1109/RAST.2017.8002959
- 900 Nygrén, T., Aikio, A. T., Kuula, R., & Voiculescu, M. (2011, May). Electric fields
901 and neutral winds from monostatic incoherent scatter measurements by means
902 of stochastic inversion. *Journal of Geophysical Research (Space Physics)*, *116*,
903 A05305. doi: 10.1029/2010JA016347
- 904 Oleynik, P., & Vainio, R. (2019). Raw simulation data of response of the PATE
905 particle telescope to electrons. [Data set]. *Zenodo*. doi: [http://doi.org/10.5281/](http://doi.org/10.5281/zenodo.2682547)
906 [zenodo.2682547](http://doi.org/10.5281/zenodo.2682547)
- 907 Palmroth, M. (2019). *Vlasiator*. Web site. Retrieved from [http://www.physics](http://www.physics.helsinki.fi/vlasiator/)
908 [.helsinki.fi/vlasiator/](http://www.physics.helsinki.fi/vlasiator/) (last access: 09.05.2019)
- 909 Palmroth, M., Ganse, U., Pfau-Kempf, Y., Battarbee, M., Turc, L., Brito, T., ...
910 von Alfthan, S. (2018). Vlasov methods in space physics and astrophysics. *Living*
911 *Reviews in Computational Astrophysics*, *4*, 1. doi: 10.1007/s41115-018-0003-2
- 912 Palmroth, M., & the Vlasiator team. (2019). *Vlasiator: hybrid-vlasov simula-*
913 *tion code*. Github repository. Retrieved from [https://github.com/fmihpc/](https://github.com/fmihpc/vlasiator/)
914 [vlasiator/](https://github.com/fmihpc/vlasiator/) (Version 3.0, last access: 09.05.2019)
- 915 Phipps, C. R., Baker, K. L., Libby, S. B., Liedahl, D. A., Olivier, S. S., Pleasance,
916 L. D., ... Valley, M. T. (2012). Removing orbital debris with lasers. *Advances in*
917 *Space Research*, *49*(9), 1283 - 1300. doi: 10.1016/j.asr.2012.02.003
- 918 Pytte, T., Trefall, H., Kremser, G., Jalonen, L., & Riedler, W. (1976, July). On
919 the morphology of energetic /not less than 30 keV/ electron precipitation dur-
920 ing the growth phase of magnetospheric substorms. *Journal of Atmospheric and*
921 *Terrestrial Physics*, *38*, 739-755. doi: 10.1016/0021-9169(76)90112-4
- 922 Reeves, G. D., McAdams, K. L., Friedel, R. H. W., & O'Brien, T. P. (2003, May).
923 Acceleration and loss of relativistic electrons during geomagnetic storms. *Geophys-*
924 *ical Research Letters*, *30*, 1529. doi: 10.1029/2002GL016513
- 925 Rodger, C. J., Kavanagh, A. J., Clilverd, M. A., & Marple, S. R. (2013, Decem-
926 ber). Comparison between POES energetic electron precipitation observations and
927 riometer absorptions: Implications for determining true precipitation fluxes. *J.*
928 *Geophys. Res. Space Physics*, *118*, 7810-7821. doi: 10.1002/2013JA019439
- 929 Saito, S., Miyoshi, Y., & Seki, K. (2010, August). A split in the outer radiation belt
930 by magnetopause shadowing: Test particle simulations. *Journal of Geophysical Re-*
931 *search (Space Physics)*, *115*, A08210. doi: 10.1029/2009JA014738
- 932 Sandroos, A. (2019). *Vlsv: file format and tools*. Github repository. Retrieved from
933 <https://github.com/fmihpc/vlsv/> (last access: 09.05.2019)
- 934 Sauvaud, J. A., Moreau, T., Maggiolo, R., Treilhou, J. P., Jacquey, C., Cros, A., ...

- 935 Gangloff, M. (2006, April). High-energy electron detection onboard DEMETER:
 936 The IDP spectrometer, description and first results on the inner belt. *Planetary*
 937 *and Space Science*, *54*, 502-511. doi: 10.1016/j.pss.2005.10.019
- 938 Seppänen, H., Kiprich, S., Kurppa, R., Janhunen, P., & Hægström, E. (2011,
 939 November). Wire-to-wire bonding of μm -diameter aluminum wires for the
 940 Electric Solar Wind Sail. *Microelectronic Engineering*, *88*, 3267-3269. doi:
 941 10.1016/j.mee.2011.07.002
- 942 Shain, C. A. (1951, September). Galactic Radiation at 18.3 Mc/s. *Australian Jour-*
 943 *nal of Scientific Research A Physical Sciences*, *4*, 258. doi: 10.1071/PH510258
- 944 Shprits, Y. Y., Angelopoulos, V., Russell, C. T., Strangeway, R. J., Runov, A.,
 945 Turner, D., ... Clemmons, J. H. (2018, February). Scientific Objectives of Elec-
 946 tron Losses and Fields INvestigation Onboard Lomonosov Satellite. *Space Science*
 947 *Reviews*, *214*, 25. doi: 10.1007/s11214-017-0455-4
- 948 Shprits, Y. Y., Subbotin, D. A., Meredith, N. P., & Elkington, S. R. (2008, Novem-
 949 ber). Review of modeling of losses and sources of relativistic electrons in the outer
 950 radiation belt II: Local acceleration and loss. *Journal of Atmospheric and Solar-*
 951 *Terrestrial Physics*, *70*, 1694-1713. doi: 10.1016/j.jastp.2008.06.014
- 952 Shprits, Y. Y., Thorne, R. M., Horne, R. B., Glauert, S. A., Cartwright, M., Russell,
 953 C. T., ... Kanekal, S. G. (2006, March). Acceleration mechanism responsible for
 954 the formation of the new radiation belt during the 2003 Halloween solar storm.
 955 *Geophysical Research Letters*, *33*, L05104. doi: 10.1029/2005GL024256
- 956 Simnett, G. M. (2011, July). Energetic neutral atoms from the Sun: an alternative
 957 interpretation of a unique event. *Astronomy & Astrophysics*, *531*, A46. doi: 10
 958 .1051/0004-6361/201116429
- 959 Spiro, R. W., Reiff, P. H., & Maher, J., L. J. (1982). Precipitating electron en-
 960 ergy flux and auroral zone conductances-an empirical model. *Journal of Geophysic-*
 961 *al Research*, *87*, 8215-8227. doi: 10.1029/JA087iA10p08215
- 962 Thorne, R. M. (1974, April). A possible cause of dayside relativistic electron precip-
 963 itation events. *Journal of Atmospheric and Terrestrial Physics*, *36*, 635. doi: 10
 964 .1016/0021-9169(74)90087-7
- 965 Thorne, R. M. (2010, November). Radiation belt dynamics: The importance of
 966 wave-particle interactions. *Geophysical Research Letters*, *37*, L22107. doi: 10
 967 .1029/2010GL044990
- 968 Thorne, R. M., & Kennel, C. F. (1971, January). Relativistic electron precipitation
 969 during magnetic storm main phase. *Journal of Geophysical Research*, *76*, 4446.
 970 doi: 10.1029/JA076i019p04446
- 971 Tsuda, Y., Mori, O., Funase, R., Sawada, H., Yamamoto, T., Saiki, T., ...
 972 Kawaguchi, J. (2013, February). Achievement of IKAROS - Japanese deep
 973 space solar sail demonstration mission. *Acta Astronautica*, *82*, 183-188. doi:
 974 10.1016/j.actaastro.2012.03.032
- 975 Tu, W., Selesnick, R., Li, X., & Looper, M. (2010). Quantification of the precipi-
 976 tation loss of radiation belt electrons observed by sampex. *Journal of Geophysical*
 977 *Research: Space Physics*, *115*(A7). doi: 10.1029/2009JA014949
- 978 Tummala, A. R., & Dutta, A. (2017). An overview of cube-satellite propulsion tech-
 979 nologies and trends. *Aerospace*, *4*(4). doi: 10.3390/aerospace4040058
- 980 Turner, D. L., Angelopoulos, V., Li, W., Bortnik, J., Ni, B., Ma, Q., ... Rodriguez,
 981 J. V. (2014, March). Competing source and loss mechanisms due to wave-particle
 982 interactions in Earth's outer radiation belt during the 30 September to 3 October
 983 2012 geomagnetic storm. *Journal of Geophysical Research (Space Physics)*, *119*,
 984 1960-1979. doi: 10.1002/2014JA019770
- 985 Tverskoy, B. A. (1969). Main mechanisms in the formation of the Earth's radia-
 986 tion belts. *Reviews of Geophysics and Space Physics*, *7*, 219-231. doi: 10.1029/
 987 RG007i001p00219
- 988 Ukhorskiy, A. Y., Anderson, B. J., Brandt, P. C., & Tsyganenko, N. A. (2006,

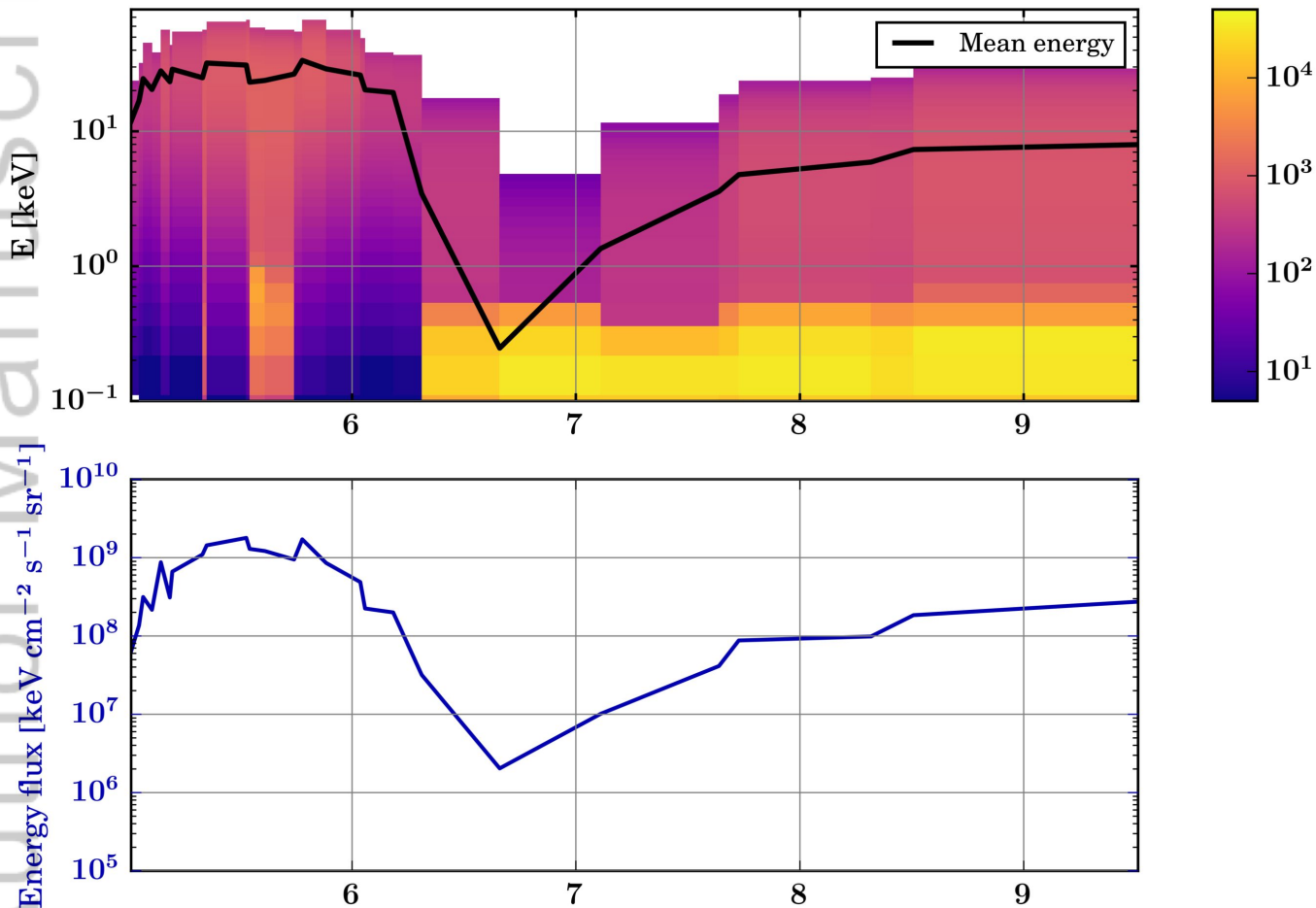
- 989 November). Storm time evolution of the outer radiation belt: Transport and
990 losses. *Journal of Geophysical Research (Space Physics)*, *111*(10), A11S03. doi:
991 10.1029/2006JA011690
- 992 van Allen, J. A., & Frank, L. A. (1959, February). Radiation Around the Earth to a
993 Radial Distance of 107,400 km. *Nature*, *183*, 430-434. doi: 10.1038/183430a0
- 994 van de Kamp, M., Seppälä, A., Clilverd, M. A., Rodger, C. J., Verronen, P. T., &
995 Whittaker, I. C. (2016). A model providing long-term data sets of energetic elec-
996 tron precipitation during geomagnetic storms. *J. Geophys. Res. Atmospheres*,
997 *121*, 12,520-12,540. doi: 10.1002/2015JD024212
- 998 von Alfthan, S., Pokhotelov, D., Kempf, Y., Hoilijoki, S., Honkonen, I., Sandroos,
999 A., & Palmroth, M. (2014). Vlasiator: First global hybrid-Vlasov simulations
1000 of Earth's foreshock and magnetosheath. *Journal of Atmospheric and Solar-*
1001 *Terrestrial Physics*, *120*, 24-35. doi: 10.1016/j.jastp.2014.08.012
- 1002 Walt, M. (1996). Source and Loss Processes for Radiation Belt Particles. *Washing-*
1003 *ton DC American Geophysical Union Geophysical Monograph Series*, *97*, 1. doi:
1004 10.1029/GM097p0001
- 1005 West, H. I., Buck, R. M., & Walton, J. R. (1972, November). Shadowing of Electron
1006 Azimuthal-Drift Motions near the Noon Magnetopause. *Nature Physical Science*,
1007 *240*, 6-7. doi: 10.1038/physci240006a0
- 1008 Woodger, L. A., Halford, A. J., Millan, R. M., McCarthy, M. P., Smith, D. M., Bow-
1009 ers, G. S., ... Liang, X. (2015, June). A summary of the BARREL campaigns:
1010 Technique for studying electron precipitation. *Journal of Geophysical Research*
1011 *(Space Physics)*, *120*, 4922-4935. doi: 10.1002/2014JA020874

Figure 1.

Author Manuscript

Electron precipitation – 00 MLT

Differential
number flux
[$\text{el cm}^{-2} \text{s}^{-1} \text{sr}^{-1} \text{eV}^{-1}$]



This article is protected by copyright. All rights reserved.

Figure 2.

Author Manuscript

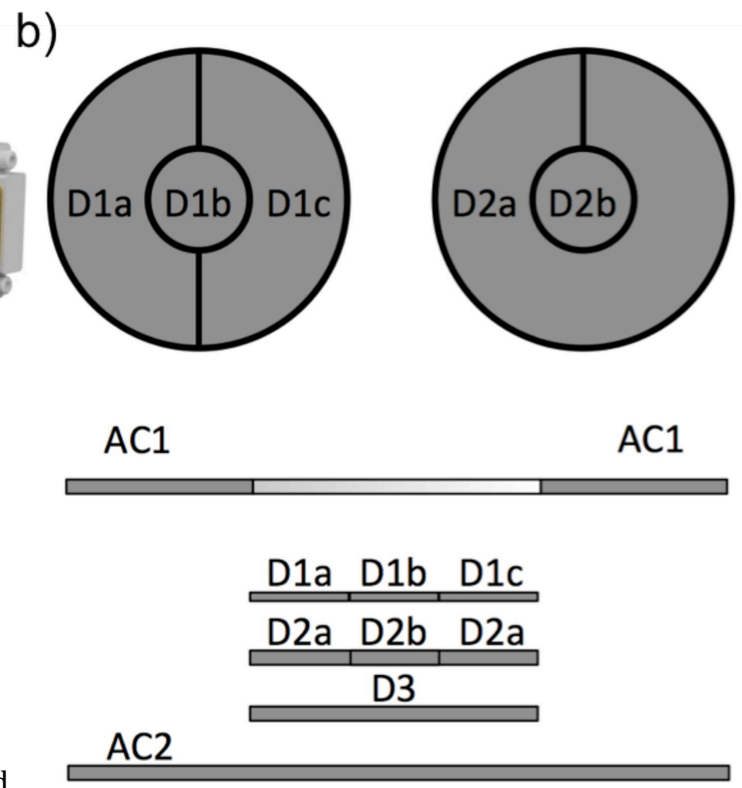
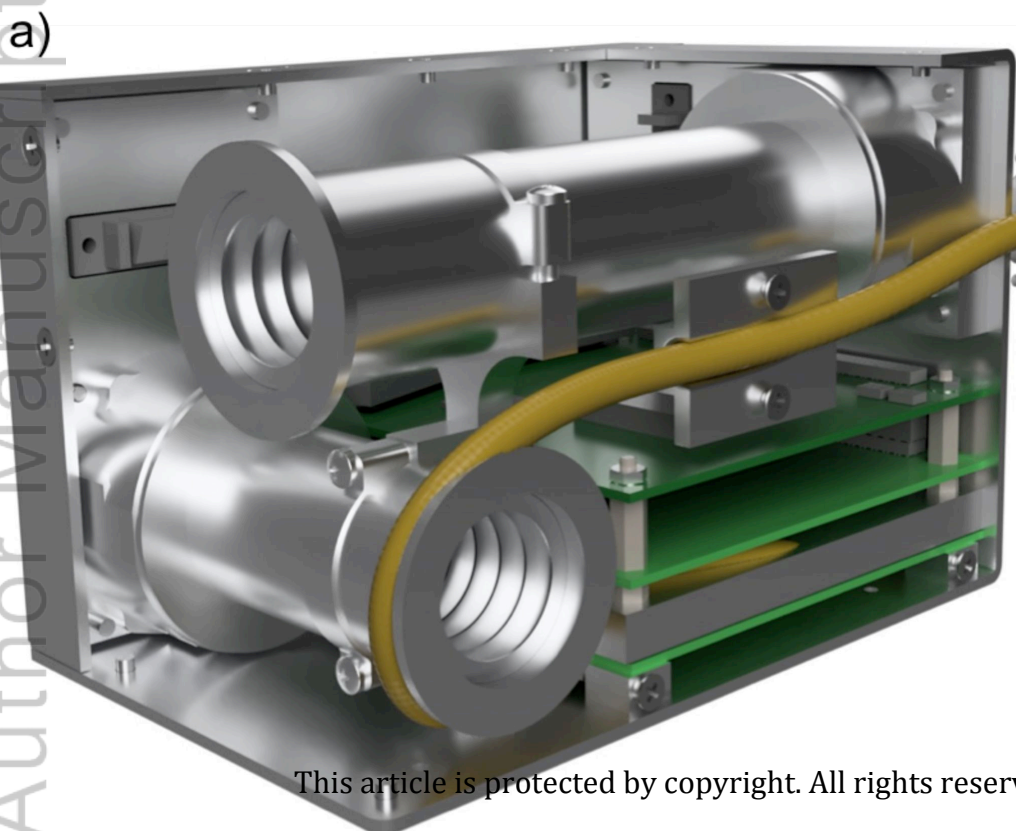


Figure 3.

Author Manuscript

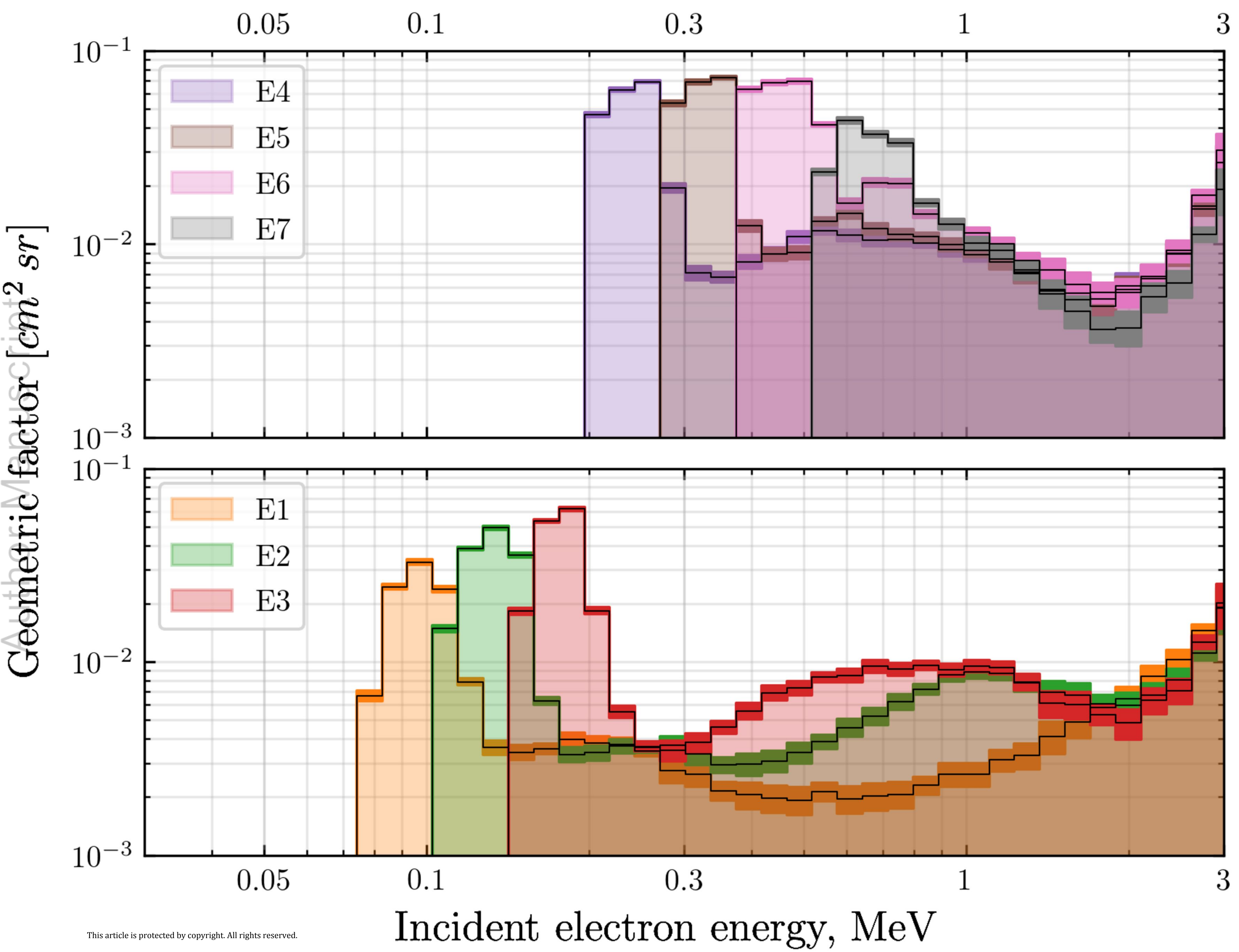


Figure 4.

Author Manuscript

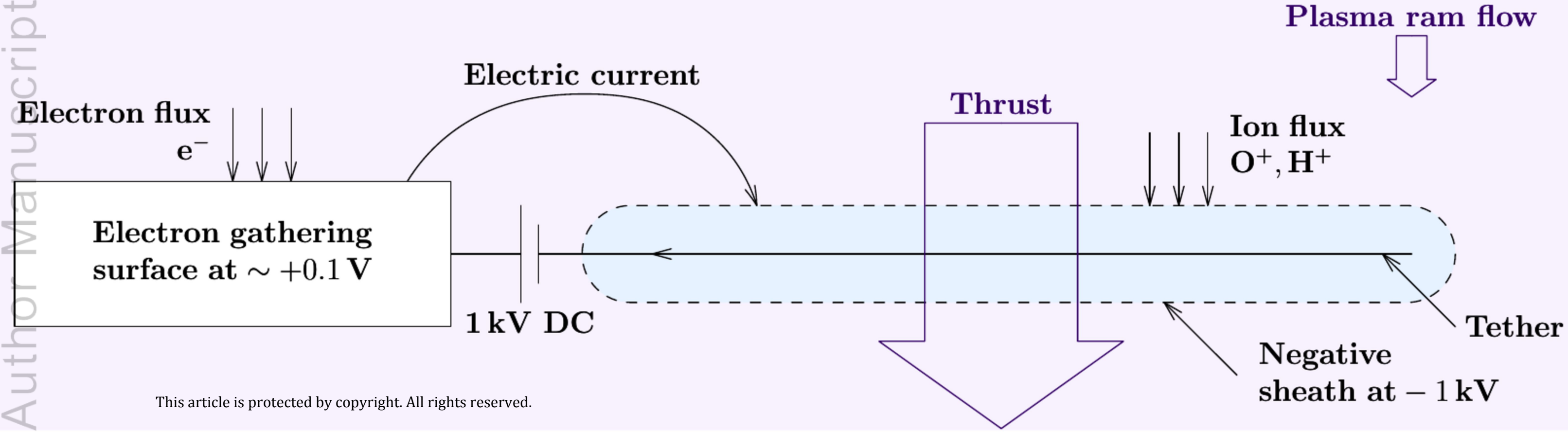
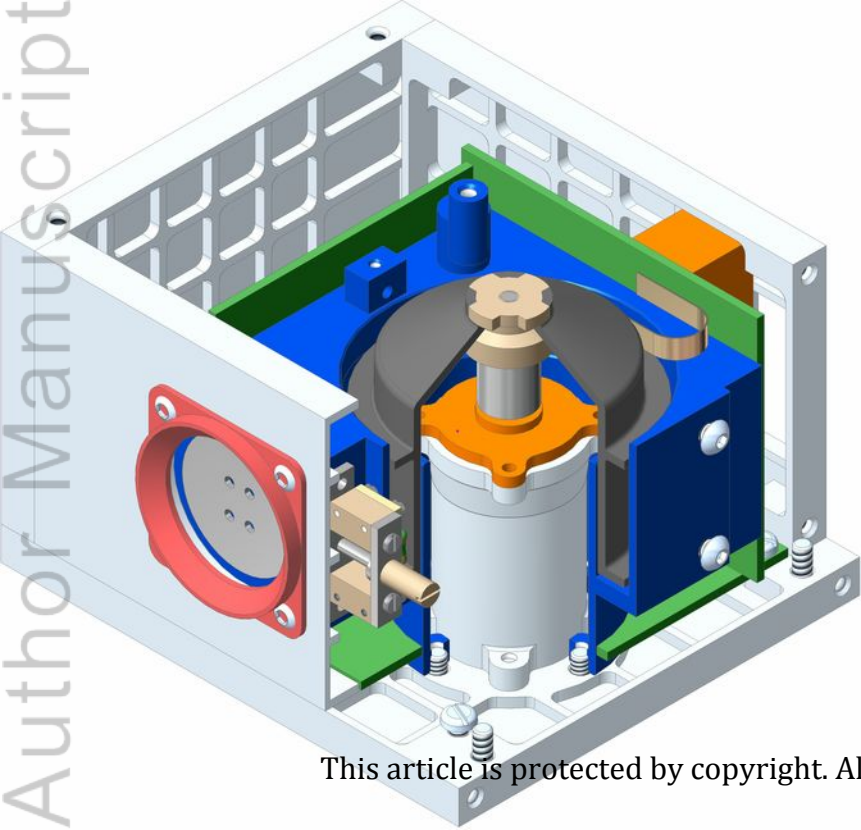


Figure 5.

Author Manuscript



Author Manuscript

This article is protected by copyright. All rights reserved.

Figure 6.

Author Manuscript

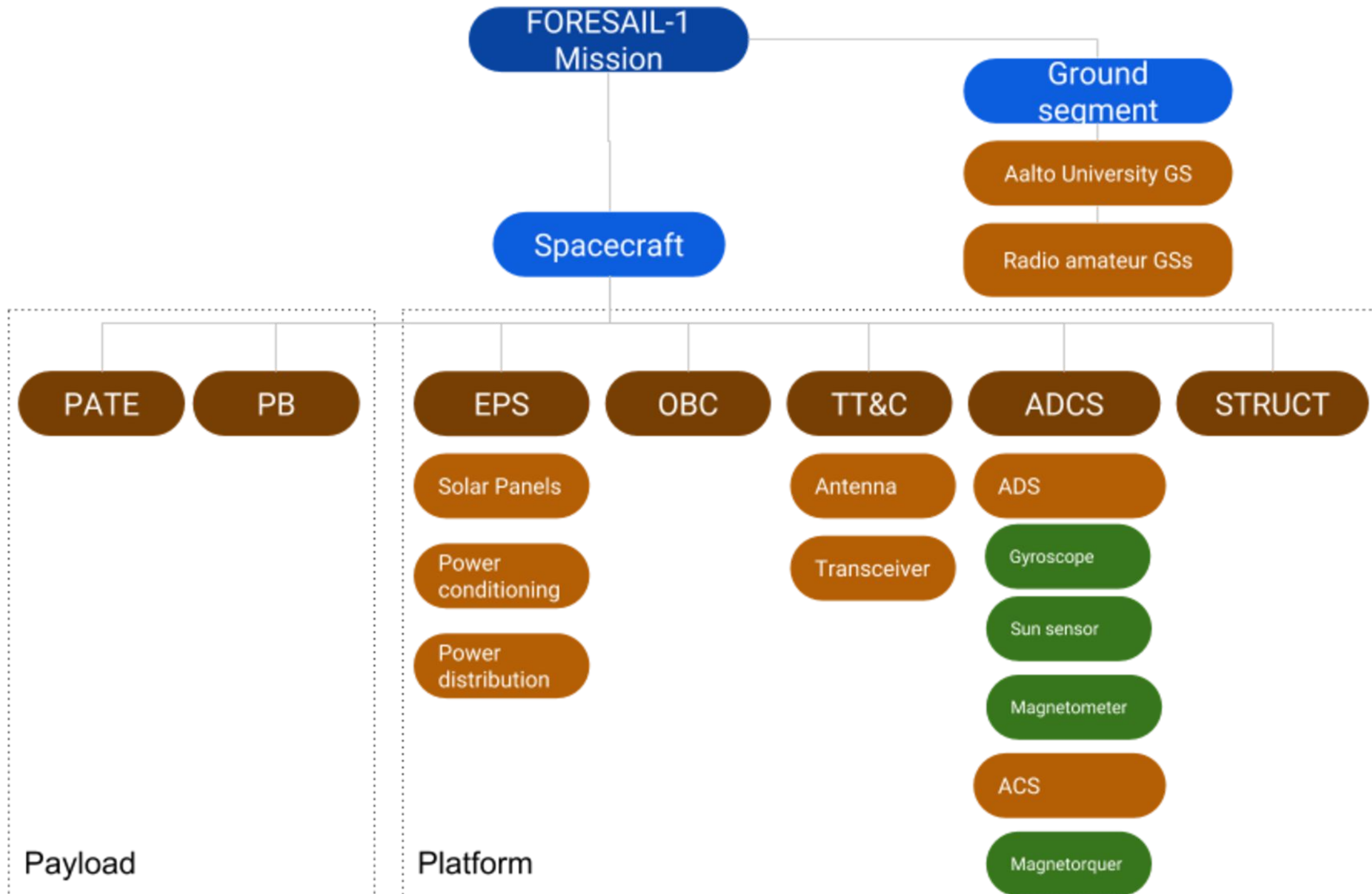


Figure 7.

Author Manuscript

Particle telescope

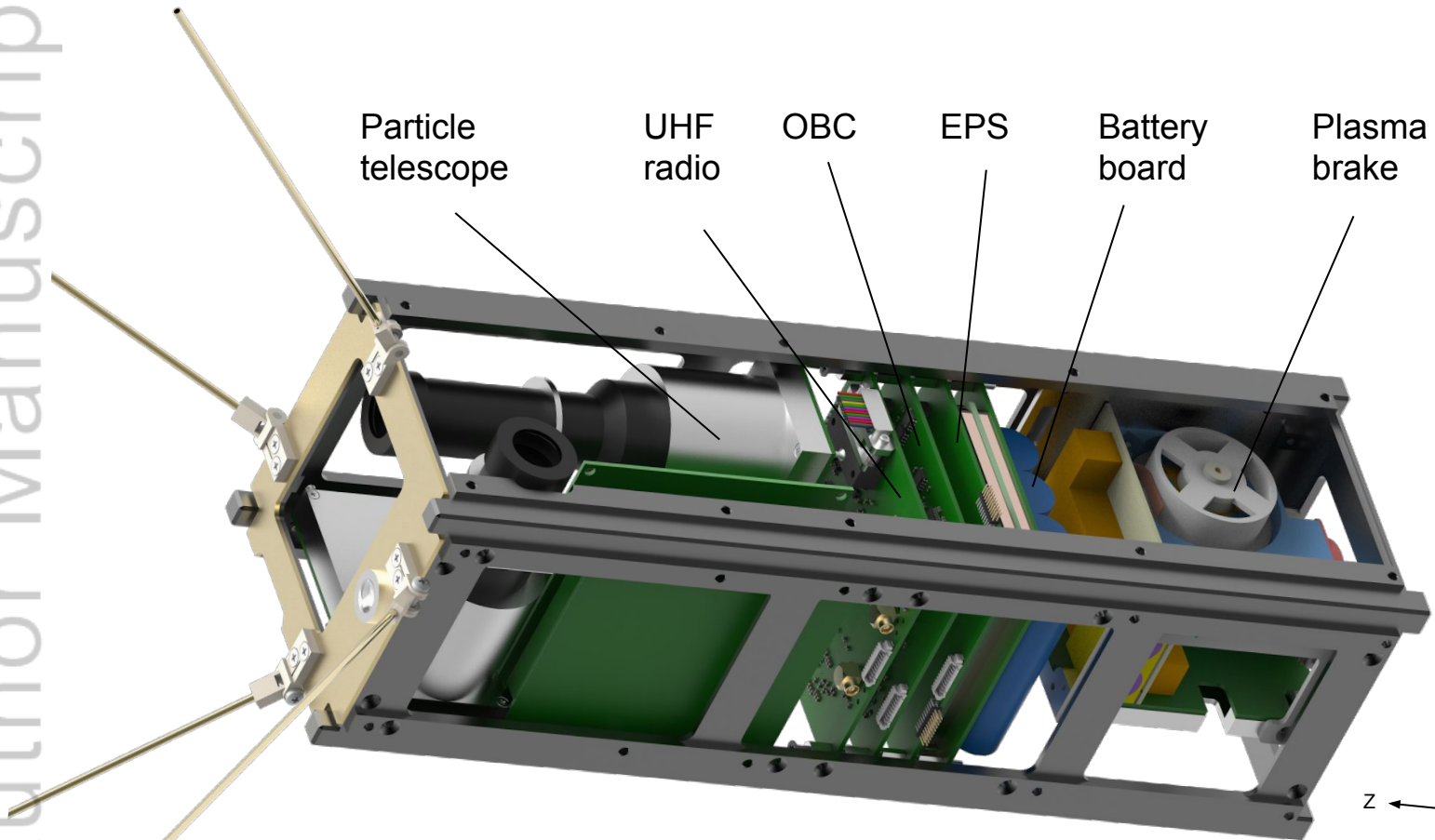
UHF radio

OBC

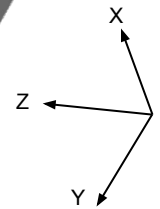
EPS

Battery board

Plasma brake

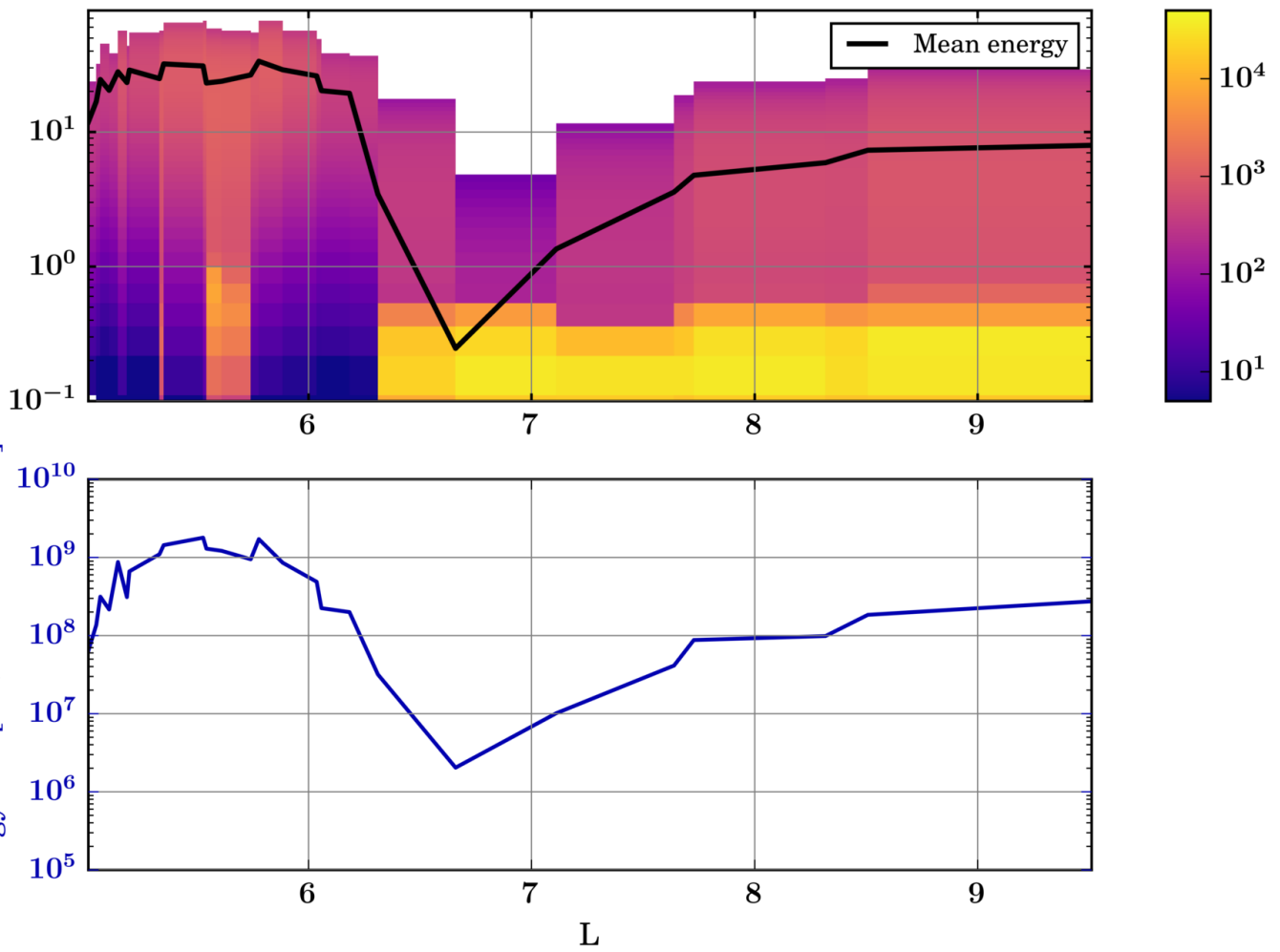


This article is protected by copyright. All rights reserved.



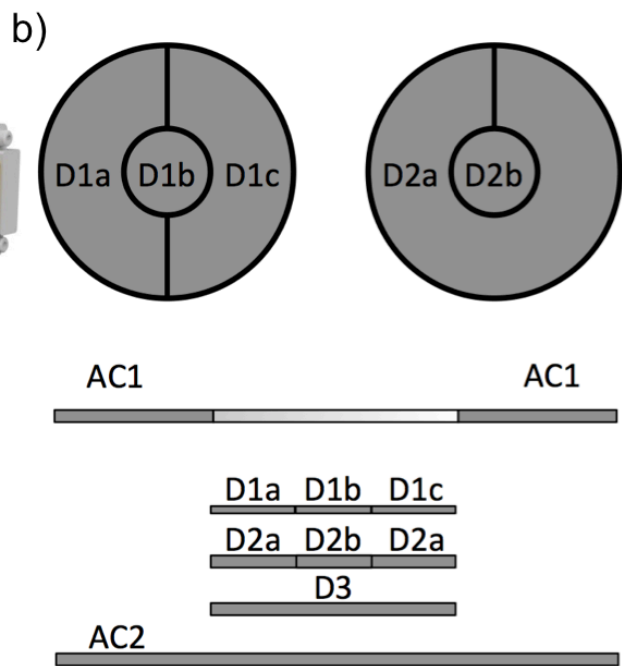
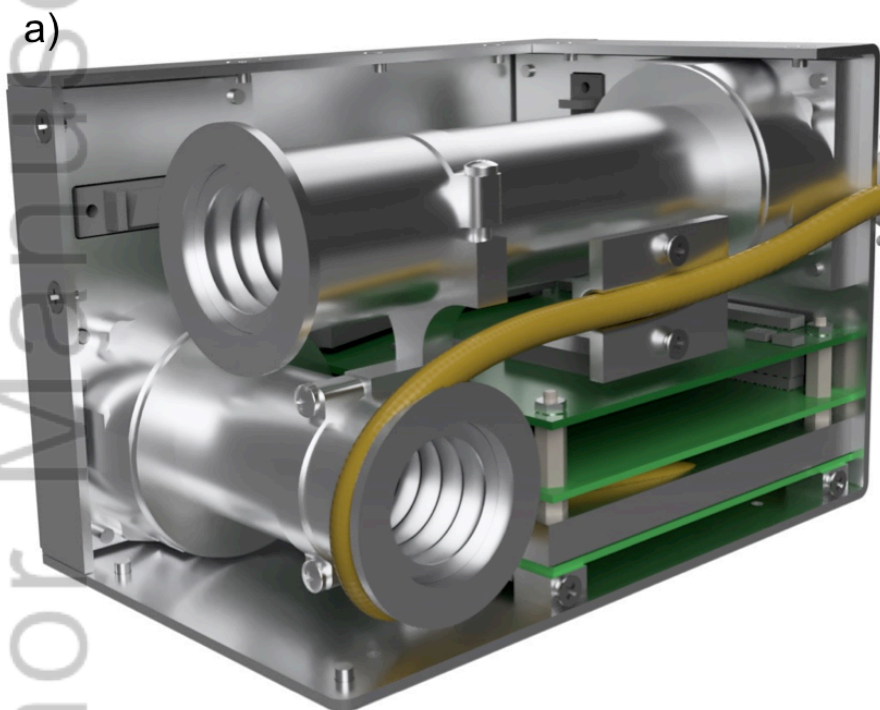
Electron precipitation – 00 MLT

Differential number flux
[$\text{el cm}^{-2} \text{s}^{-1} \text{sr}^{-1} \text{eV}^{-1}$]

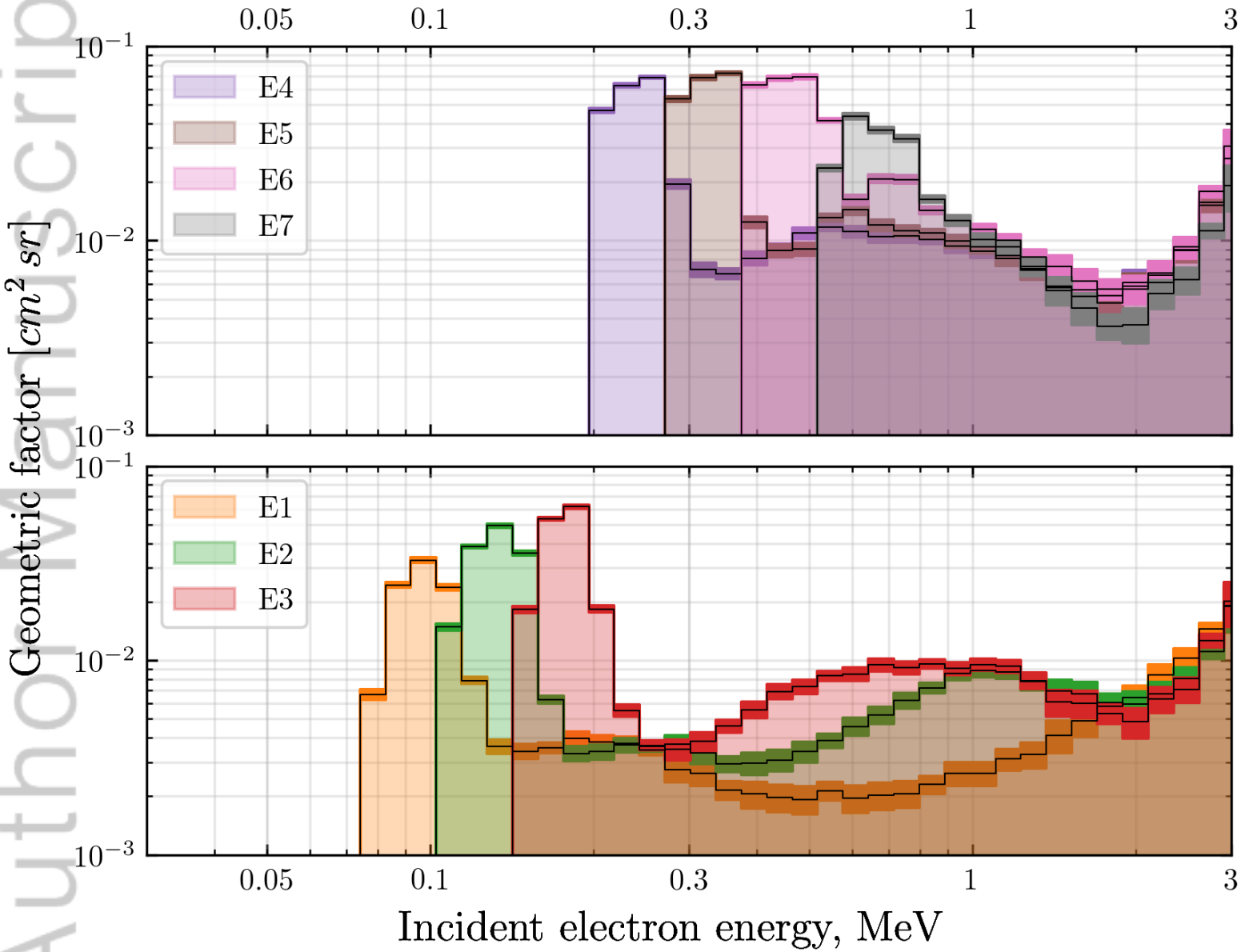


2018JA026354-f01-z-.png

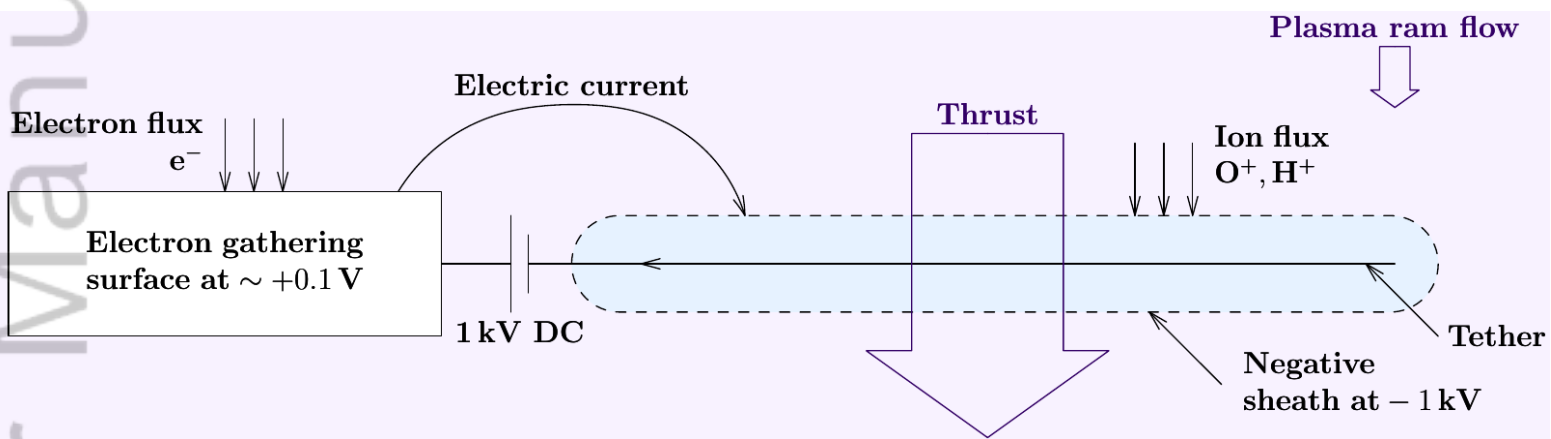
Author Manuscript



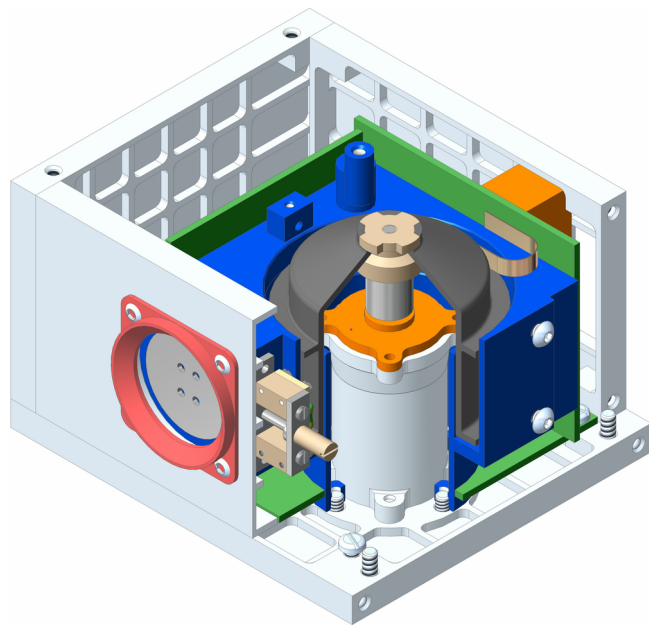
2018JA026354-f02-z-.png



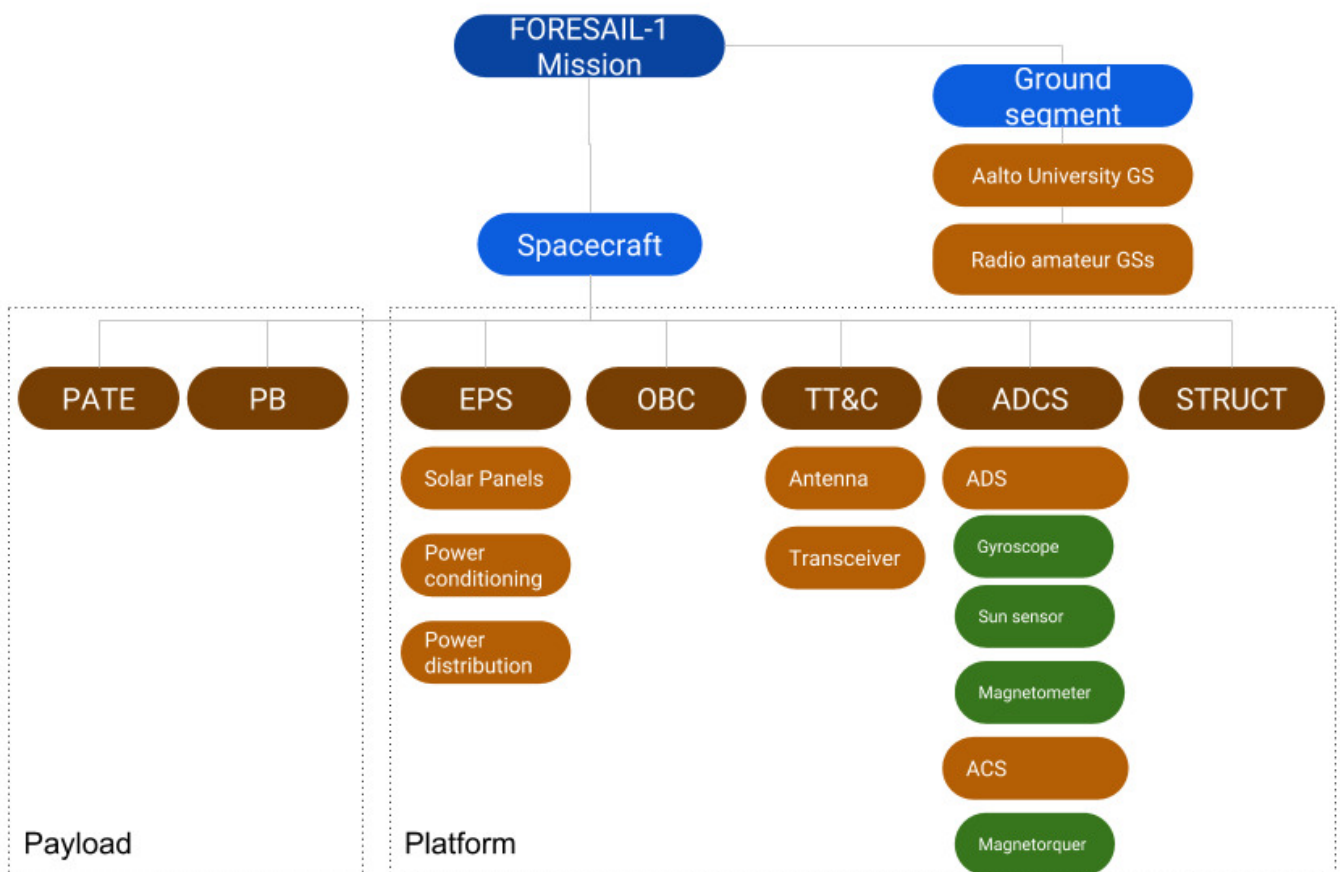
2018JA026354-f03-z-.png



2018JA026354-f04-z-.png



2018JA026354-f05-z-.png



2018JA026354-f06-z-.jpg

Particle telescope

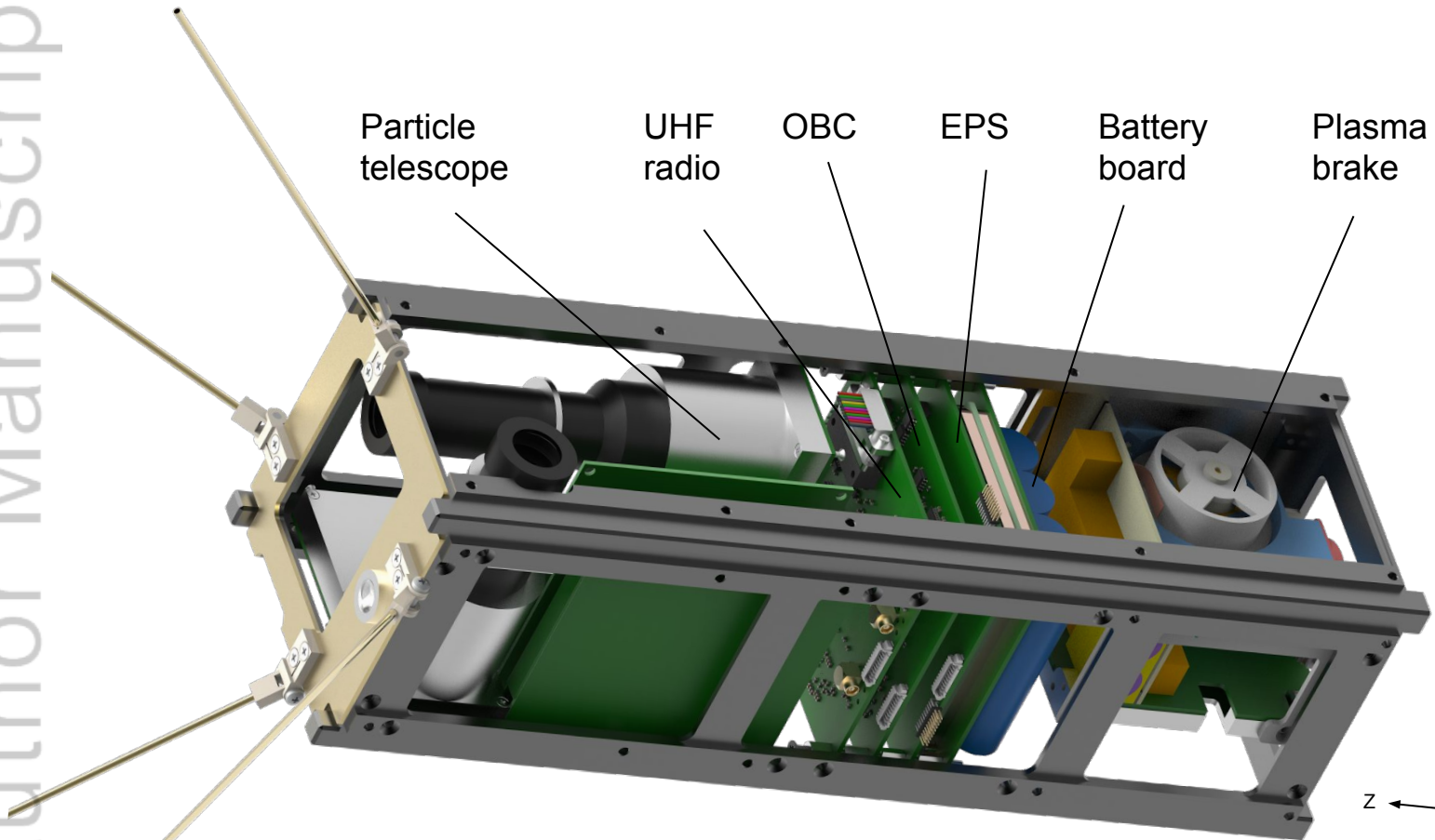
UHF radio

OBC

EPS

Battery board

Plasma brake



This article is protected by copyright. All rights reserved.